Microfluidics and Nanofluidics (2022) 26: 80
https://doi.org/10.1007/s10404-022-02587-3

REVIEW

Recent hypotheses on the parameters of microchannel flow boiling: a comprehensive overview

K. R. Balasubramanian[1] · R. John Peter[1] · R. Ajith Krishnan[2]

Received: 6 June 2022 / Accepted: 31 August 2022 / Published online: 19 September 2022

Abstract

In recent decades, microchannel flow boiling has been prioritised in thermal management compared to conventional methods due to its superior heat transfer capability and high surface area-to-volume ratio. However, the instability and fluctuation of flow boiling in microchannels indicate a lack of understanding in boiling characteristics, preventing this application from being commercialized. In addition, despite the fact that flow pattern-based models have been developed in recent decades, it has not been possible to anticipate all the flow boiling heat transfer data using a generalised model or correlation. This paper begins with a contradictory notion regarding the mechanism of microchannels compared to macrochannel flow boiling. Then, flow behaviour and mechanisms of boiling characteristics in microscale channels are reviewed, including design, operational, and thermo-physical aspects. So that the effect of the characteristics can be evaluated and incorporated into the heat transfer/HTC correlation to improve accuracy, as their behaviour in the microchannel is complex and nonlinear due to bubble confinement and flow pattern. Finally, the effects of design, operation, and thermo-physical parameters on microchannel heat transfer are studied in terms of physical phenomena, mechanisms, and flow structures.

Keywords Heat transfer coefficient (HTC) · Instability · Micro-channel · Flow boiling and flow behaviour

List of symbols

D_h	Hydraulic diameter (mm)
h	Heat transfer coefficient (HTC) (W/m^2°C)
G	Mass flux (kg/m^2)
P	Pressure (N/m^2)
q	Heat flux (W/m^2)
T	Temperature (K/°C)

Greek symbols

σ	Surface tension (N/m)
θ	Contact angle

Non-dimensional number

Nu	Nusselt number
Re	Reynolds number

Subscripts

l	Liquid
sat	Saturated (K/°C)
sub	Subcooled (K/°C)
sup	Superheat (K/°C)

Abbreviations

CHF	Critical heat flux (W/m^2)
x	Vapour quality
AR	Aspect ratio
ONB	Onset nucleate boiling
VUF	Vertical upward flow

1 Introduction

According to the International Roadmap for Devices and Systems 2021, the thermal power dissipation of electronic devices remains a major growth constraint. Midway through the previous decade, the power dissipation of microprocessors reached fundamental limits of 120–130 W. The operational frequency could no longer be increased despite the fact that transistor performance could have easily enabled circuits to operate at tens of gigahertz (GHz) or more (www.ieee.org and https://irds.ieee.org). It is anticipated that electronic devices will exceed the heat flux dissipation rate of 1 kW/cm^2 due to the increased number of transistors per unit area in electronic chips and defence application power

✉ K. R. Balasubramanian
krbala@nitt.edu

[1] Department of Mechanical Engineering, National Institute of Technology, Tiruchirappalli, India

[2] School of Mechanical Engineering, Sungkyunkwan University, Gyeonggi-do, South Korea

modules. This need for cooling electronics in industrial applications has prompted research into microchannel flow boiling, a promising future application (Kandlikar 2005; Kandlikar et al. 2005; Karayiannis and Mahmoud 2017).

A cooling system for a microscale device requires cooling channels of a few micrometres as opposed to conventional channels. When the size of the microchannels is 10–100 µm, it is exceedingly difficult to directly measure the flow rate or velocity of the flow, which necessitates the size range of 1–3 mm for research studies (Kandlikar et al. 2005). Chen et al. (2006) identified micro- and macrochannels (1.1–4.26 mm) using the flow pattern transition, where the flow pattern recorded in the macrochannel (bubble, slug, churn, annular, and mist flow) was entirely different from the flow pattern observed in the microchannel (confined bubbles, thin liquid film surrounding the vapour slug, and absence of mist). There is also consensus that lowering the diameter greatly affects the flow pattern, which has an effect on the heat transfer process and the heat transfer coefficient (HTC). Thus, the microchannel term may be applied when the channel size approaches the bubble departure diameter, resulting in behaviours that are distinct from those observed in macrochannels. Figure 1 shows the flow boiling parameters.

Regarding the microchannel heat transfer mechanism, numerous researchers have reported contradictory results as nucleate boiling (Bao et al. 2000; Anwar et al. 2014), convective boiling (Qu and Mudawar 2003; Boye et al. 2007; Mortada et al. 2012), both nucleate and convective boiling (Mahmoud et al. 2009; Lin et al. 2001; McNeil et al. 2013), and others as thin-film evaporation mechanisms (Huh and Kim 2006; In and Jeong 2009; Ali et al. 2012; Balasubramanian et al. 2013) as dominant mechanism in microchannel flow boiling. Inferring the nucleate boiling contribution, when the HTC rises with increasing heat flux and system pressure, regardless of mass flow and vapour quality (Bao et al. 2000). Alternately, it is convective boiling if the HTC rises with increasing mass flux and vapour quality, but is unaffected by heat flux (Qu and Mudawar 2003). Figure 2 depicts the schematic of the different mechanisms proposed in the literature.

In addition to nucleate and convective boiling, understanding the formation of a liquid/thin film between the annulus (after bubble merger) and the wall is essential for understanding the microchannel phase-change mechanism (Bigham and Moghaddam 2015). The thin-film region is governed by capillary and disjoining pressures where solid–liquid molecular interaction results in a drop

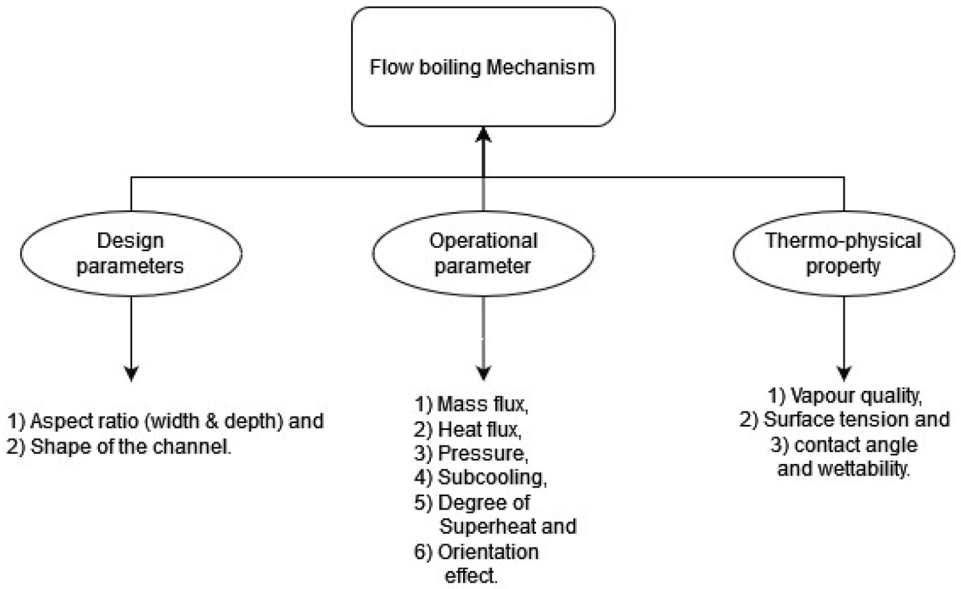

Fig. 1 Parameters affecting microchannel flow boiling mechanism

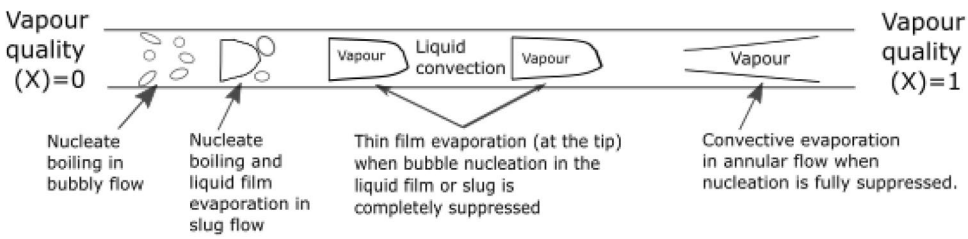

Fig. 2 Schematic of different mechanisms on microchannel flow boiling (Karayiannis and Mahmoud 2017)

in liquid pressure and a relatively low vapour pressure (Park et al. 2003). Based on this, liquid pressure fluctuation dominates over vapour pressure in the development of thin films. Upon further examination of the liquid–vapour interface of bubbles, it was determined that the bubble merging process enhances wall heat transfer by arresting the liquid film between the bubble and the wall underneath the bridges and vapour neck before departure (Ling et al. 2015; Sun 2019). In addition, 30–70% of total evaporation is contributed by microlayer evaporation, which significantly influences heat transfer (Luo et al. 2020a; Utaka et al. 2018). Yet, Basu et al. (2011) stated that there is no general agreement on the dominant heat transfer mechanism in a microchannel due to the lack of studies into the operational and thermo-physical variables.

Aside from this contradictory mechanism, using a microchannel will result in a higher frictional pressure drop due to the confined bubble growth in both single-phase and multi-phase flow. It causes rapid evaporation, flow reversal, and instabilities in multi-parallel microchannel configurations (Kandlikar 2004). In addition to these design parameters, these unstable modes (instability) were also affected by operating and physical parameters, such as contact angle, wettability, surface tension, superheat, and mass flux (Wu and Cheng 2004; Bogojevic et al. 2009; Bogojevic et al. 2011; Diaz and Schmidt 2007). Flow instability and flow reversal are also caused by the rate of bubble growth caused by heat and mass transfer and two-phase oscillation (Bogojevic et al. 2013; Huh and Kim 2013; Celata et al. 2012). However, all the primary heat transfer and instability behaviours, such as bubble clogging, reversal, departure before full development, and dry-out, are the function of operating parameters, such as mass flow rate, wall heat flux, inlet subcooling, pressure, and saturation temperature.

Owing to the investigation of microchannel flow boiling over the last 2 decades, the research revealing its fundamental mechanism through its operational parameters in two-phase flow is still vast. Even though the researchers are striving to reveal its mechanism in particular operating conditions, the generalised view has not been found (Tibirica and Ribatski 2013; Cheng and Xia 2017). In this study, the design, operational, and thermo-physical characteristics necessary for understanding microchannel two-phase boiling behaviour are thoroughly examined. Priority is given to observing flow behaviour in microchannels over correlations made by various researchers, as many of these correlations are not universally applicable due to operating range limits. Also, since numerous theories have offered the science underlying this process, the results have been compelled to examine the most recent hypothesis within their operational range. This will provide the investigators with in-depth knowledge of the design, operation, and thermo-physical properties of a microchannel flow boiling in the state of the art.

2 Design parameters of flow boiling

2.1 Aspect ratio [AR] (width and depth)

The aspect ratio (AR) of microchannels affects boiling incipience and nucleation characteristics due to the channel walls' constraints on bubble growth in the transverse direction. These constraints lead to a large gradient of velocity and temperature profile near the wall, which is rendered by the thermo-capillary force (variation of surface tension; Ghiaasiaan and Chedester 2002). In further, the appearance of this microbubble (early nucleation) influences the boiling process by accelerating the onset of nucleate boiling (ONB) at lower superheats. The bubbly flow's size decreases in the microchannels due to the low inertia, enhanced surface tension, and viscous effects. In the width range of 100–5850 µm in a rectangular channel, the flow regime is said to differ (HTC raises) up to 400 µm in a rectangular microchannel at a constant depth (Chung and Kawaji 2004). When the width was increased even more, the flow regime and the heat transfer coefficient (HTC) did not change. The schematic of the parallel rectangular channel with aspect ratio is shown in Fig. 3.

With the increase in channel size, the liquid film is retarded due to the thermal inertial effect. This leads to a considerable time delay in the conductive heat transfer that occurs in the liquid film region. Whereas, when the width of the channel was smaller, the liquid film got thinner, enhancing effective heat conduction across the liquid film (Magnini and Thome 2016). Additionally, it is essential to note that when the liquid film gets thinner with AR, it makes the frictional pressure drop higher. Singh et al. (2008) explain that the pressure drop varied non-linearly

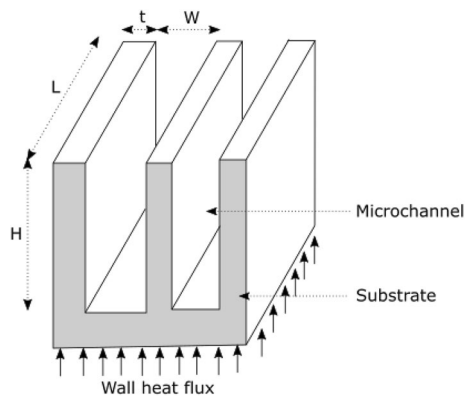

Fig. 3 Schematic diagram of a straight parallel rectangular channel, aspect ratio defined as width (*W*)-to-height (*H*) ratio

with the aspect ratio (width and depth), imposing a minimum pressure drop. The mass flux (G) diminishes monotonically as AR increases. As the acceleration pressure drop is proportional to G^2, it decreases the pressure drop (due to mass flux reduction). Since the acceleration and friction pressure drop work against each other, the overall pressure drop is lowest with AR. However, the higher HTC obtained is transient due to the variation of thermal inertia in the liquid film and the cyclic transit of slug and liquid pair.

Further examination of the microchannel's cross-sectional area (0.088 mm^2) revealed the absence of bubbly flow (Harirchian and Garimella 2009a, b). Since the liquid slug with a high contact surface is more difficult to break, it takes more energy to disperse the bubble's gas phase in a small volume, necessitating a high Reynolds number for the transition from slug flow. Vapour confinement in these microchannels (slug flow) results in larger values of HTC as the heat transfer comprises both nucleate boiling and liquid film evaporation mechanisms. Thus, in many experimental studies (Sahar et al. 2017; Zhang et al. 2011), the HTC increases as the diameter/width of the channel decreases.

The corner (amount of liquid in the corner) and the adiabatic length effect determined the optimal AR for a higher HTC. The amount of liquid in the corner increases up to the optimum AR and then decreases (Markal et al. 2016a). Physically, the bubble size was increased with a lower aspect ratio due to the confinement effect and heat transfer around the walls. Where slug flow occurs, decreasing the pressure drop with an enhanced HTC (Al-Zaidi et al. 2021). Also, when the hydraulic diameter was changed from 0.1 to 1 mm at a fixed AR, the hydrodynamic entry length (the distance from the entrance of the channel to the point where the velocity is 99% of its fully developed value) did not change (Sahar et al. 2017).

The average Nusselt number declines with decreasing D_h and increasing AR. However, the rise in AR is limited because of the velocity profile change from parabolic to flattened (Raj et al. 2019). It is evident from the discussion that bubble confinement and the formation of a thin liquid film region improve the thermal performance of microchannels in low AR. However, because of the mass flux at low AR, the total pressure was greater compared to high AR. Despite the precision of the AR mechanism, the flow loop effect, the number of channels, and the adiabatic length were found to influence heat transfer and instability (Li et al. 2018a), which must be experimentally documented as there is no universal flow regime model based on channel dimensions. The selected literature on the impact of dimension is provided in Table 1.

2.2 Channel shape and configuration

The straight-channel heat sink improves the heat dissipation from electronic devices, but the huge temperature difference between the upstream and downstream sides of the channel reduces its longevity and reliability. Many authors have achieved higher thermal performances with corresponding pressure drop by varying the shape of the channel, like circular, rectangular, trapezoidal, V-grooved, diverging/converging, expanding shaped, etc. Before discussing the channel shapes, it is worth mentioning that increasing the area ratio or restricting the inlet in the desired flow direction can reduce the reverse flow and explosive bubble growth (Mukherjee and Kandlikar 2009; Li and Hrnjak 2017). When both the entrance and exit conduits were placed perpendicular to the microchannel, the amplitude and pressure fluctuation in reversed flow were increased. However, on restricting the only inlet (perpendicular to the inlet and parallel to the outlet), the connection shows no oscillation, reverse flow, or pressure fluctuation of the vapour bubble. This configuration was suggested for higher heat flux applications to avoid significant temperature fluctuations and early burn-out (Wang et al. 2008).

Yogesh et al. (2015) observed higher HTC and negligible pressure drop on segmented channel heat sinks than straight and divergent channels due to the breaking of the thermal boundary layer, enhanced mixing, and the availability of more nucleation sites. Different bubble growth patterns were observed in segmental channels, resulting in either condensing or flushing out in their early growth stages (Prajapati et al. 2017a), leading to lower temperature fluctuations at the bottom wall than in other channels. However, the pumping power is said to rise exponentially with the mass flow rate of water in the segmented microchannel, resulting in a higher pressure drop (Prajapati et al. 2017b). At 30 g/s, the pressure drop of the segmental channel was 30 Kpa, which was approximately 10 times greater than the pressure drop of the straight-channel heat sink. However, for electronic cooling, the minimum temperature variation is the priority. To achieve a variation in temperature of less than 5 °C, a straight channel requires 100 g/s with a pressure loss of 23 Kpa. However, the segmental channel requires only 15 g/s with only 8.5 Kpa, which is 2.8 times less than the straight channel. In short, the pressure drop penalty in implementing segmented flow was appropriate, providing a higher Nusselt number than a straight channel for the same pressure drop (Betz and Attinger 2010). Many researchers (Bhandari and Prajapati 2021; Hedau et al. 2020; Naqiuddin et al. 2018) optimised fin width, height, number of channels, and mass flow rate in straight and segmental channels, which were the best options for electronic devices with a high heat flux.

Table 1 Summary of the impact of channel dimension on microchannel flow boiling

Author	Working fluid	Channel dimensions/cross-sectional area	Parameter constraints	Key observation
Chung and Kawaji (2004)	Nitrogen, gas, and water	D_h 50–530 µm	–	50 and 100 µm Channel shows variation in flow pattern
Harirchian and Garimella (2009a)	FC-77	Widths 100–5850 µm, and depth 400 µm	G: 225–1420 kg/m^2 s	Critical width 400 µm
Harirchian and Garimella (2009a)	FC-77	Depth 100–250 µm and Width from 100 to 1000 µm	G: 630 kg/m^2 s	Critical cross-section 0.089 mm^2
Zhang et al. (2011)	Water, ethanol, three sodium carboxy-methyl cellulose and SDS	D_h 302, 496 and 916 µm and 10 cm length	T_{sub}: 25 °C	Higher flow transition with lower channel diameter
Sahar et al. (2017)	Water	D_h 0.1–1 mm with fixed AR 1. AR 0.39–10 of D_h 0.56 mm	Re = 100–2000	D_h contributes larger than AR, in HTC
Magnini and Thome (2016)	R245fa	D_h 0.3–0.7 mm	G = 400–700 kg/m^2 s, q'' = 5–20 kW/m^2 and T_{sat} 10–50 °C	Liquid film thickness is the reason for enhanced HTC
Singh et al. (2008)	De-ionized water	AR: 1.23–3.75	D_h = 142 ± 2 µm, L = 20 mm	Min. pressure drop at AR 1.56
Markal et al. (2016a)	De-ionized water	AR: 0.37–5.00	D_h = 100 µm, G: 151–324 kg/m^2 s and q": 71–131 KW/m^2	$AR_{optimum}$: 1.22
Mohiuddin et al. (2020)	De-ionized water	AR: 0.31, 0.92 and 3.7	D_h = 0.6 mm, l = 40 mm, G: 270–650 kg/m^2 s, q'': 200–620 KW/m^2	$AR_{optimum}$: 0.31
Cheng et al. (2021)	De-ionized water	AR: 1, 2.5 and 4	Depth: 15–45 µm, G: 446–963 kg/m^2 s, q'': 36.2–427.9 W/cm^2 and T_{sat}: 100 °C	$AR_{optimum}$: 2.5
Al-Zaidi et al. (2021)	HFE-7100	AR: 0.5, 1 and 2	D_h = 0.46 mm G: 50–250 kg/m^2 s, q'': 9.6–191.6 KW/m^2	$AR_{optimum}$: 2

Al-Neama et al. (2017) investigated three distinct multi-serpentine configurations with straight rectangular microchannels (SRM): a single-path multi-serpentine microchannel (SPSM), a double-path multi-serpentine microchannel (DPSM), and a triple-path multi-serpentine microchannel (TPSM). The SPSM exhibits higher Nusselt numbers than other channels due to the frequency of channel bends that disrupt the thermal boundary layer (a small region of circulating flow is created near the inner surface of the bend). This facilitates the effective heat transfer from the walls to the water, reducing the wall temperature. However, when looking at overall performance, the SPSM needs more pumping power to get a high HTC, while the TPSM gets a better thermal performance with less pumping power. However, in the analysis by Cheng et al. (2020), the sinusoidal wave profile (wavy-insert, wavy-heater, wavy-serpentine in an annular microchannel with a 300 µm gap) was utilised. The single-walled wavy channels outperformed the serpentine and straight channels due to the flow area constriction in wavy-walled passages, which resulted in a greater velocity gradient and enhanced fluid mixing due to the increased friction factor.

Zhang et al. (2016) proposed the interconnected microchannel net (IMN), where the combination of a re-entrant structure and sharp corners at the intersection is responsible for its superior performance. The bubble growth instability is suppressed as a result of the re-entrant cavities in the IMN, which provide a high density of nucleation and enhance the system's stability by reducing the required wall superheat. At the intersection, the sharp corners shear the expanding bubble moving downstream and break it into smaller bubbles. This occurs whenever the thermo-hydraulic boundary is broken, which stabilises bubble formation. Thus, the IMN attained higher heat flux and lower pressure drop due to inconsequential two-phase instability (Ling et al. 2019). The schematics of various shapes of the channel suggested by the researchers are provided in Fig. 4.

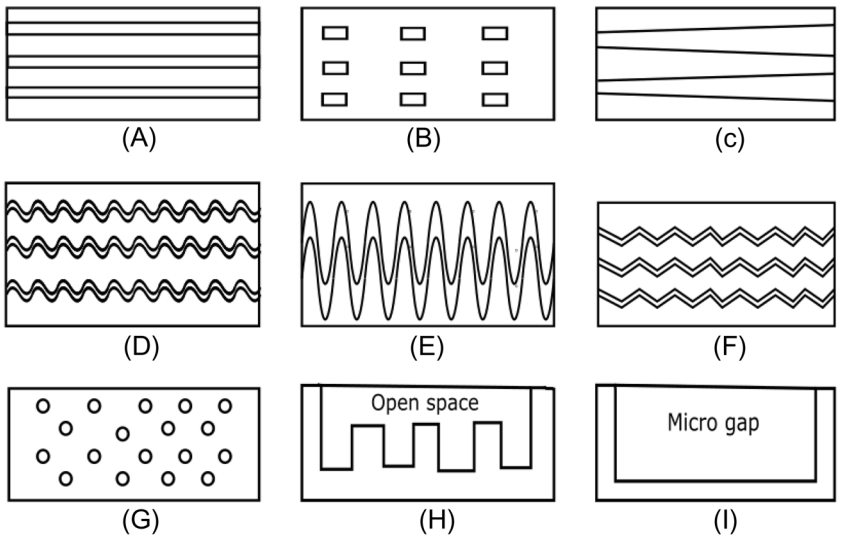

Fig. 4 Top view of (**a**) straight parallel (Prajapati et al. 2015), (**b**) segmental (Prajapati et al. 2017b), (**c**) divergent (Prajapati et al. 2015; Lin et al. 2011), (**d**) wavy (Cheng et al. 2020), (**e**) serpentine (Al-Neama et al. 2017), (**f**) Zig-zag rectangular MCHS (Ma et al. 2019), (**g**) Circular micro-pin–fin (Kong et al. 2020) and front view of (**h**) open (Balasubramanian et al. 2018; Mathew et al. 2020) and (**i**) micro-gap MCHS (Krishnan et al. 2018; Ajith Krishnan et al. 2018)

Ma et al. (2019) conducted experiments with offset zigzag cavities in a microchannel heat sink. Compared to rectangular microchannels, zigzag cavities generate a higher HTC due to the cavity's disturbance, delaying coalescence, flow reversal, and partial dry-out by preserving wettability. Using de-ionized water as the working fluid, Kong et al. (2020) analysed micro-pin–fin shapes, such as circular, diamond, and oval. Due to their geometries (larger surface area for diamond and oval microfins), the required heat flux was greater for diamond and oval microfins than for circular microfins. However, the required wall superheats for the ONB are the same for all micro-pin fin heat sinks (Bhandari and Prajapati 2021).

From the discussion on microchannel configuration, the researchers have improved the heat transfer while incurring a pressure drop penalty by breaking the thermal boundary layer using sharp bends, corners, wavy paths, etc. However, the applicability of the microchannel is contingent on the need for temperature priority. It is evident from the discussion that microchannels like segmental, TPSM, Wavy, IMN, etc. have surpassed rectangular microchannels in thermal performance with a pressure drop penalty. Apart from the closed microchannel, researchers proposed the micro-gap (open) channel, because bubbles can expand in the spanwise direction and travel downstream without causing flow reversal effects. As a result of this, the vapour slug from neighbouring microchannels coalescences with each other as they expand. In the micro-gap section, the coalesced vapour slug expands and evacuates towards the exit. Despite the improvement in boiling stability, the reduced heat transfer resulted in higher wall temperatures, which triggered partial dry-out and accelerated CHF. The performance of the hybrid heat sink (microchannel + micro-gap) is superior to that of the micro-gap heat sink but inferior to that of the straight heat sink (Balasubramanian et al. 2018; Mathew et al. 2020), despite its higher boiling stability and lower pressure drop (Mathew et al. 2019). Numerous authors have investigated numerically diverse configurations, such as manifold arrangement (Z, C, H, and U) (Luo et al. 2020b), forward-and backward-facing steps (Yuan et al. 2020), radial curved microchannel (Mamidi et al. 2021), and double taper microchannel (Mahesh et al. 2021), etc. Table 2 displays the effects of various shapes on heat transfer with constraints.

3 Operating parameters of flow boiling

3.1 Mass flux (*G*)

The thermal boundary layer thickness, which is the most important characteristic for heat transfer, is sensitive to changes in the imposed mass flux. Increased mass flux/flow velocity increases incipient heat flux by delaying nucleation, which is governed by both nucleate and convective boiling (Collier and Thome 1994). The liquid is superheated at the nucleate boiling point to maintain bubble nucleation and growth. The bubbles will be suppressed along the wall during forced convective boiling, resulting in the thin annular liquid film being carried away by evaporation at the liquid interface. Figure 5 depicts a schematic of both nucleate and convective boiling.

A bubble will grow beyond the mouth of the cavity only when its surrounding liquid is sufficiently superheated; the boiling incipience is found to be dependent on both bubble growth and departure (Qu and Mudawar 2003). However, the nucleation rate declines progressively with mass flux in the forced convection boiling region (Qu and Mudawar 2002). The reason for this delayed bubble nucleation was explained by Revellin and Thome (2007). On increasing the mass flux in the microchannel, the

Table 2 Summary of the shape and configuration of channels in microscale application

Authors	Working fluid	Shape modification	Parameter constraints	Key observations
Wang et al. (2008)	Water	(a) Both entry and exit was restricted, (b) no restriction and (c) entry alone restricted	$L = 30$ mm, $D_h = 186$ µm, $q = 184.2–485.5$ kW/m^2	The Type-C connection was recommended for high heat flux microchannel
Prajapati et al. (2015)	DI-water	Uniform, diverging and segmented finned micro-channels	$G = 100–350$ kg/m^2 s and $q = 10–350$ kW/m^2	Segmented finned channels have high HTC than others
Prajapati et al. (2017a)	DI-water	Uniform, diverging and Segmented finned micro-channels	$G = 100–350$ kg/m^2 s, $q = 10–350$ kW/m^2 and $D_h = 522$ µm	Segmented finned channels have reduced flow instability
Naqiuddin et al. (2018)	Water	W_F (1–4), L_F (1–4), L_{TF} (2–5), N (1–3), W_C (0.3–1) and m (10–20 g/s)	Subcooling 56.6 °C, pumping power of 0.13 W using 15 g s^{-1}	Optimised result: W_F—1 mm, L_F—2 mm, L_{TF}—5 mm and W_C—1 mm
Bhandari and Prajapati (2021)	Water	Fin height 0.5–2 mm	Reynolds number 100–800 with heat flux 75–150 KW/m^2	Optimum height 1.5 mm
Zhang et al. (2016)	DI-water	Interconnected microchannel net	Inlet subcooling of 10, 40 and 70 K	Achieved high heat transfer than others
Al-Neama et al. (2017)	Water	SRMs, SPSMs, DPSMs and TPSMs	Pressure 0–2.1 bar	SPSM showed enhancement (35%) compared with SRM
Ling et al. (2019)	DI-water	Interlaced (IM), parallel (PM) and spiral microchannel (SM)	–	Heat transfer performance of IM was higher
Kong et al. (2020)	DI-water	Circular, diamond, and oval micro-pin fin heat sinks	$G = 147.4–355.4$ kg m^{-2} s^{-1} and $q = 4.8–55.8$ W cm^{-2}	Heat flux required for ONB is higher for diamond and oval
Ma et al. (2019)	Acetone	Zig-zag cavities	$G = 285–684$ kg/(m^2 s) and $q = 1.31–80.26$ W/cm^2	Fluctuating amplitude decreases with heat flux
Kingston et al. (2018)	HFE-7100	Single microchannel with uniform heat flux	$D_h = 500$ µm, $\Delta T_{sub} = 5–35$ °C, G 200–800 kg/m^2 s	Low flow inertia causes severe temperature raises
Kwon et al. (2019)	R245fa	High-power density microchannel	Re. no: 7500–20,500, $G = 330–750$ kg/m^2 s	High-power density 180 W/cm^3 in 1 cm^3
Luo et al. (2020b)	HFE-7100	Manifold microchannel (Z-type, C-type, H-type and U-type)	$T_{sub} = 7$ K. $q_w = 0–200$ W/cm^2	H and U shows lower pressure drop than other types
Hedau et al. (2020)	DI-water	6, 10 and 14 parallel microchannel	Footprint area: 1×1 cm^2, $G = 500$ kg/m^2 s and $q = 220$ W/cm^2	14 parallel microchannel higher HTC (240%)
Loganathan et al. (2020)	Water	Bypass inlet	$2.5 \times 0.6 \times 25$ mm^3, 30–850 kg/m^2 s and $q = 87–548$ kW/m^2	HTC increases with the by-pass ratio
Yuan et al. (2020)	FC-72	Backward-facing and forward-facing step	The expansion ratio of 2, 2.5 and 3. Reynolds number 3048-6097. T_{sub} 35 K	Backward facing has low heat transfer

flow pattern transition tends to be faster from bubbly to elongated bubble due to the quick coalescence. In other words, the higher the mass flux, the earlier annular flow is reached, leading to a thicker liquid film (min. liquid film thickness is more important than average liquid film thickness in triggering dry-out phenomena). Therefore, liquid film thickness increases with mass flow, because the liquid moves rapidly and the thickness of the liquid film varies with time, resulting in a decrease in HTC (Magnini and Thome 2016). Figure 5 and Table 3 show how mass flow changes when some parameters are fixed in microscale applications.

Concerning various inflow velocities with a constant heat flux, bubble nucleation frequency increased monotonically with inflow mass. As mass velocity increased, bubble size distribution along the channel tended to become flatter (Youn et al. 2015; Farahani and Karami 2019; Ghosh et al. 2012; Yuan et al. 2019; Wu and Wang 2021; Bhuvankar and Dabiri 2020). Thus, it can be concluded from the scientific literature that mass flux has a significant effect on the onset

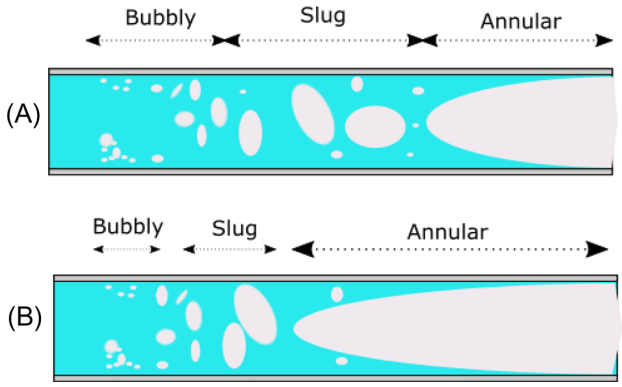

Fig. 5 Schematic of flow pattern behaviour for **a** nucleate boiling dominant—HTC depends on heat flux and **b** convective boiling dominant—HTC depends on mass flux

of nucleate boiling, with an increase in mass flux necessitating an increase in heat flux to initiate nucleation. Furthermore, it plays a significant role in liquid film thickness and accelerated flows.

3.2 Heat flux (*q*)

The contribution of heat flux to the nucleate-dominant boiling mechanism in microchannels (Liu et al. 2005; Bertsch et al. 2009; Saisorn et al. 2018) is substantial. This impacts the ONB by early nucleation depending on flow rate, liquid subcooling, and contact angle (Basu et al. 2002). As the heat flux increased, ONB was activated, and the location was observed to shift upstream. The HTC increases linearly with increasing heat flux and becomes predominately nucleate at high heat flux (Bertsch et al. 2009; Deng et al. 2015).

At lower heat fluxes, bubble nucleation was inhibited, but at high heat fluxes, bubble coalescence at a higher rate led to an annular transition where the liquid film becomes thinner, improving heat transfer (Harirchian and Garimella

Table 3 Summary of mass and heat flux effect on microchannel flow boiling

Authors	Working fluid	Heat flux and mass flux	Parameter constraints	Key observation
Bertsch et al. (2009)	R-134a and R-245fa	0–22 W cm^{-2} and 20–350 kg m^{-2} s^{-1}	D_h = 1.09—0.54 mm, x = −0.2–0.9, T_{Sat} = 8–30 °C	HTC has strong dependence on heat flux
Harirchian and Garimella (2009a)	FC-77	33.7–250 kW/m^2 and 225–1420 kg/m^2 s	D_h = 100–5850 µm, with a depth of 400 µm	Dominated nucleate boiling
Deng et al. (2015)	De-ionized water	25–430 KW/m^2 and 160–300 kg/m^2 s	D_h = 671 µm, 786 µm and 871 µm. Inlet temperatures 90 °C	Strong dependence of heat flux
Magnini and Thome (2016)	De-ionized water	5–20 KW/m^2 and 200–500 kg m^{-2} s^{-1}	Only in slug flow	HTC decreases with heat flux
Zhang et al. (2016)	De-ionized water	Max. 542 kW m^{-2}	Width = 0.25, 0.4 and 0.55 mm and T_{sub} 40 K	Influence of flow transition
Li et al. (2018b)	De-ionized water	4–20 W/cm^2 and 120–360 kg/m^2 s	X = 0.03–0.1	HTC decreases with heat flux
Liu and Wang (2019)	De-ionized water	80–160 kW/m^2 and 400 kg/(m^2 s)	D_h = 0.4 mm, T_{sat} = 304.15 K	Strong dependence of heat flux
Jagirdar and Lee (2020)	De-ionized water	28.9–94 W/cm^2 and 200–1000 kg/(m^2 s)	Height = 0.14, 0.28 and 0.42 mm,	Raises nucleation frequency in surge of HTC
Bertsch et al. (2009)	R-134a and R-245fa	0–22 W/ cm^2 and 20–350 kg/m^2 s	D_h = 1.09 and 0.54 mm and T_{sat} = 8–30 °C	Weak function of mass flux
Revellin and Thome (2007)	R-134a and R-245fa	3.2–422.1 KW/m^2 and 200–2000 kg/m^2 s	D_h = 0.5–0.8 mm and T_{sat} = 26, 30 and 35 °C	Earlier transition of flow pattern
Young et al. (2015)	Water, ethanol and FC-40	Water 2.47 m/s, ethanol 0.263 m/s	D_h = 1 mm and length of 500 mm	Mass flux plays a dominant role
Saisorn et al. (2018)	R-134a	1–60 kW/m^2 and 250–20 kg/m^2 s	D_h = 1 mm and P_{sat} = 8 bar	Mass effect was negligible at orientation
Farahani and Karami (2019)	Water and nano-fluid as water–copper	200 W and 20, 165, 350, 440 and 580 kg/m^2 s	Incoming water at 60 °C	Wall temp, HTC and x were depended on mass flux
Yuan et al. (2019)	FC-72	0.5 m/s	D_h = 8.57 mm and T_{sub} = 35 K	Pulsating flow has higher bubbles than steady flow leads to a decline in CHF

2009a). The transition interval between bubble nucleation in wall cavities and bubble departure from the wall is referred to as the bubble growth rate, which varies linearly with heat flux (Wang et al. 2011). With an increase in heat flux, the bubble lift-off radius, frequency, and coalescence rate increased, resulting in early flow transitions (Zhuan and Wang 2012). During these types of heat transfer, the local heat flux increased rapidly when the rear end of the bubble was relocated and rewetted (Bigham and Moghaddam 2015). Also, at constant bubble frequency, the HTC drops marginally with increasing heat flux due to a thicker liquid film caused by increased acceleration (Magnini and Thome 2016). In addition, the transition from bubbly to annular flow is accompanied by boiling heat transfer, which increases the heat flux, depending on the extent of the confinement effect (bubble size reaches the channel diameter). Figure 5 depicts the flow pattern behaviour of the dominant mass and heat flux effects.

On examining the impact of heat flux in the annular region, a higher wall heat flux results in a higher HTC due to the trailing bubble it creates. The bubble's expansion in the annular zone will result in a notch at the end of the annulus; this produces a tiny droplet with a rapid growth rate that improves the HTC in the thin-film region (Liu and Wang 2019; Jagirdar and Lee 2020). In contrast to mass flow, which delays nucleation, heat flux increases ONB by initiating nucleation. However, if the mass flux is too low, dry-out processes will occur, which will increase the wall temperature. Apart from that, an increase in heat flux resulted in an increase in nucleation frequency via wall temperature with the higher flow regime transition, which led to an increase in HTC. Table 3 shows the effect of both mass and heat flux within the operating constraints below.

3.3 Pressure (*P*)

Flow instability and oscillation are the obstructions to microchannel flow boiling's practical application. System pressure is one of the essential and responsible factors for instability and flow oscillation associated with pumping power, which has not been studied at the microscale exclusively. Developing knowledge about these deleterious phenomena at the microscale is an important task. The total pressure drop on a microscale includes sudden contraction, expansion, frictional, and acceleration pressure drops. The boiling was initiated with rapid bubble formation at low pressure, resulting in rigorous flow oscillation. This large magnitude of oscillations results in an early transition to the CHF following the ONB. However, after ONB, a stable boiling zone at high pressure was identified, which maintained heat flux until the onset of boiling instability accompanied by significant temperature fluctuations (Kuo and Peles 2009). In addition, the liquid-to-vapour ratio will decrease, thereby decreasing the void fraction. As the void fraction is closely related to density wave oscillation, it delays the instability. Due to this, the bubble departure diameter is decreased (decline in bubble growth oscillation), preventing the premature transition to an unstable region and a rapid transition to CHF, thereby reducing the two-phase flow friction and momentum pressure drop. The variation of pressure with flow fluctuation and reverse flow is shown in Fig. 6.

The growth period from the small radial bubble to an elongated vapour slug was investigated by analysing the bubble confinement effect (Barber et al. 2010). This growth rate and confinement of vapour bubbles lead to an over-pressure in the microchannel, effectively creating the vapour blockage and leading to a sharp pressure fluctuation at the inlet and outlet. Most bubbles merge with the nearby ones to form larger ones. The fluctuation decreases when the elongated slug growth occurs, proving that the growth rate and bubble diameter vary inversely with pressure, because the pressure outside the vapour bubble opposes its growth due to evaporation (Katiyar et al. 2016; Wei et al. 2011).

The experimental observation made by Dario et al. (2016) demonstrates that the frequency of pressure drop fluctuation is dependent on both heat and mass fluxes. With an increase in heat flux, larger amplitude frequencies occur in the high-frequency zone, but in a single phase, the increase in heat flux decreases pressure due to low viscosity and channel blockage; flow cannot occur, necessitating additional energy at high pressure. In addition to increasing the heat flux, increasing the speed of the flow also increases the

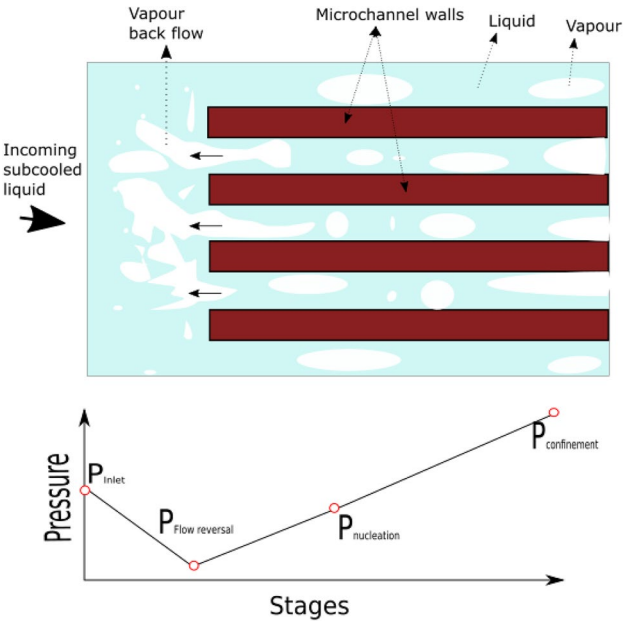

Fig. 6 Schematic representation of the pressure variation along with the reverse flow and flow fluctuation inside microchannel (Qu and Mudawar 2003)

acceleration pressure (Wang et al. 2011; Dario et al. 2016; Markal et al. 2016b).

Investigation of Keepaiboon et al. (2016) using R134a in a single rectangular microchannel proves that the total pressure drop is mostly influenced by frictional pressure drop, which was found to be dependent on heat flux and saturation temperature. From the discussion, increasing the heat flux affects the vapour quality and flow velocity, leading to higher interfacial and wall shear stress, causing a rise in frictional pressure gradient. The decrease in saturation temperature increases the frictional pressure gradient due to an increase in specific volume, causing the velocity of the refrigerant to increase. This proves that the frictional pressure gradient increases with increasing heat flux but varies inversely with saturation temperature. In addition, the increase in mass flux leads to a sudden expansion pressure drop and acceleration pressure drop. Apart from this, some other parameters found in the literature affecting the pressure system are the shear force by vapour slug expansion, channel number, length, type of refrigerant, inlet subcooling, etc. (Li et al. 2018a; Keepaiboon et al. 2016; Huang and Thome 2017; Choi and Kim 2011; Jiang et al. 2019). Table 4 provides a summary of the effects of pressure in selected literature.

3.4 Subcooling (T_{sub})

Subcooled and saturated flow boiling are the two most common boiling regimes seen in flow boiling (Collier and Thome 1994). In subcooled boiling, the temperature of the bulk fluid will be lower than its corresponding saturation temperature. The heat transfer mechanism comprises high liquid convection and bubble formation along the channel walls, both of which influence ONB flow instability (Kandlikar et al. 2005). In a microchannel, subcooling (over a given length) and saturation boiling (over the remaining length) can occur simultaneously. The more often subcooling occurs, the higher the initial heat flux needed for nucleation. Therefore, by increasing the fluid's inlet temperature, the required heat flux for ONB can be decreased (Qu and Mudawar 2002; Liu et al. 2005), demonstrating that subcooling is a function of velocity and functional dependency of heat flux (Wojtan et al. 2006; Hsieh et al. 2002). So that, at a lower subcooling, boiling commences at a lower superheat, whereas in a highly subcooled liquid, the bubble is greatly inhibited and expands slowly. Thus, the inlet subcooling has a significant impact on bubble departure, coalescence, and generation frequency. The schematic representation of the dominant mechanism in subcooled and saturated boiling is shown in Fig. 7.

At different system pressures (5–10 bar), the effect of subcooling (T_{sub} = 6–12 °C) in the parallel channel was investigated. At low pressure and subcooling (5 bar and 6.6 °C), two-phase flow oscillations with a large amplitude were observed. The amplitude and nature of the oscillation change as the mean mass flow rate decreases with increasing subcooling (12 °C). It can also be observed that the amount of subcooling required to stabilise the system at low pressure (5 bar) was greater than at high pressure (10 bar). This study by Saikia et al. (2019) indicates that, at a fixed pressure and input power, there is a range of inlet subcooling above or below which instability begins to occur. In which, flow instability is complicated by large amplitude (mixed oscillation) at low inlet subcooling. For greater subcooling, the flow oscillation assumes a peculiar form with diminished amplitude.

Sinha et al. (2019) observed that increasing the mass flow rate and degree of subcooling (2.5–8.5 °C) at a constant heat flux decreases bubble size. At highly subcooled conditions, the heat transfer rates from the heated surface were higher (due to the predominance of forced convection), which reduced the surface temperature regardless of the mass flow rate. After the initial growth of the bubble, the condensation phenomena at the bubble interface dominate the evaporative rate at the heater surface, resulting in stunted bubble growth. It is also noticeable that increased subcooling reduces bubble cycle time (short residue time) in comparison to low subcooling. As a result, the bubble separates from the heater surface and condenses, resulting in an increase in the heat flux required for the formation of confined bubble growth. The heat flux dependence disappears with the bubble elongation rate, but increases with early stage mean free bubble growth (Yin et al. 2014; Chen et al. 2019). Furthermore (with an increase in subcooling), the flow oscillation can be reduced due to a delay in slug flow as a result of decreased bubble formation and coalescence. Consequently, the average HTC rises with an increase in fluid inlet temperature and falls with subcooling (Ramesh et al. 2019), as the bubble departure and lift-off growth rates increase with inlet temperature (Sinha et al. 2019; Abdous et al. 2019).

Also, at lower inlet subcooling, the formation of a vapour bubble at the surface of the channel was accompanied by explosive bubble growth, resulting in the bubble occupying most of the channel's area and causing a pressure spike. At higher subcooling, the incoming liquid quickly refills the channel and cools the heated wall, resulting in a decreased wall temperature and a delayed transition in the flow pattern. This reduces the effect of rapid bubble growth instability, resulting in a shorter duration of flow reversal (Kingston et al. 2018; Lee and Karayiannis 2020; Zhang et al. 2021). It is clear from the analysis that only a limited number of studies exist for critical subcooling parameters. In terms of heat transfer, the lower subcooling demonstrates a higher bubble development rate with large amplitude oscillations, resulting in an increase in HTC. In contrast, more subcooling causes slower bubble generation and a drop in HTC. Apart from this, the subcooling has a crucial influence on bubble

Table 4 Key observation on the effect of pressure with parameter constraints

Authors	Working fluid	Pressure range	Parameter constraints	Key observation
Kuo and Peles (2009)	Water	50–205 kPa	Diameter 223 µm, mass fluxes 86–520 kg/m^2 s	High frequency of oscillation at high system pressure
Barber et al. (2010)	FC-72	Amplitude fluctuation of 106 mbar to − 66 mbar	Diameter 727 µm, AR 10, uniform heat flux 4.26 kW/m^2 and mass flow rate: 1.33×10^{-5} kg/s	Confined bubble growth leads to sharp pressure fluctuation
Chiwoong and Kim (2011)	Water–liquid and nitrogen–gas	0.1–1 MPa	Hydraulic diameters 141, 143, 304, 322 and 490 µm, liquid superficial velocities 0.06–1.0 m/s	Developed correlation for HFM and SFM
Wang et al. (2011)	FC-72	Pressure drop: − 9 to 30 mbar	Diameter 727 µm, aspect ratio 10, sat. temperature 56 °C, mass flux 8.75–175 kg/ms, heat flux 0–15.03 KW/m^2	Fluctuation frequency increases with heat flux and decreases with mass flux
Dario et al. (2016)	R134a	600–900 kPa	Subcooling 1–20 K, heat flux 5–220 kW m^{-2}, vapour quality 0–0.95 and mass 250–1000 kg m^{-2} s^{-1}	The pressure drop increases with mass velocity and decreases with pressure
Markal et al. (2016b)	De-ionized water	5–13 Kpa	29 Parallel square microchannel with diameters 150 µm, mass flux 51–92.6 kg/m^2 s and heat flux 9.3–84.1 kW/m^2 and Inlet temperature 50 ± 1 °C	Pressure drop generally decreases with increasing mass flux for a constant value of the heat flux
Keepaiboon et al. (2016)	R134a	Pressure drop at 16–30 Kpa	Hydraulic diameter 0.68 mm, Heat flux 7.63–49.46 kW/m^2, mass flux range 600–1400 kg/m^2 s, and sat. temperature 23–31 °C	The frictional pressure gradient increases with mass flux but is reduced with Sat. temperature
Huang and Thome (2017)	R1233zd, R245fa and R236fa	200–265 kPa	Mass fluxes from 1250 to 2750 kg m^{-2} s^{-1}, heat fluxes 20–64 W cm^{-2}, vapour quality 0.51	R236fa exhibited lower pressure drop and the increased inlet subcooling increases the pressure drop
Li et al. (2018a)	R134a	10–60 Kpa/m	Inlet temperature 16 °C, mass flux 373–1244 kg/m^2 s, heat flux 132–407 KW/m^2	The shear force by the vapour slug as the reason for the frictional pressure drop
Jiang et al. (2019)		Flow pattern based on amplitude–frequency	Hydraulic diameter 526.2 µm, heat flux 11.58–99.56 kW/m^2, mass flux 20.40–107.04 kg/m^2 s and inlet temperature T_{in} = 55 °C	Oscillation frequency follows the V shape (increase and then decrease)

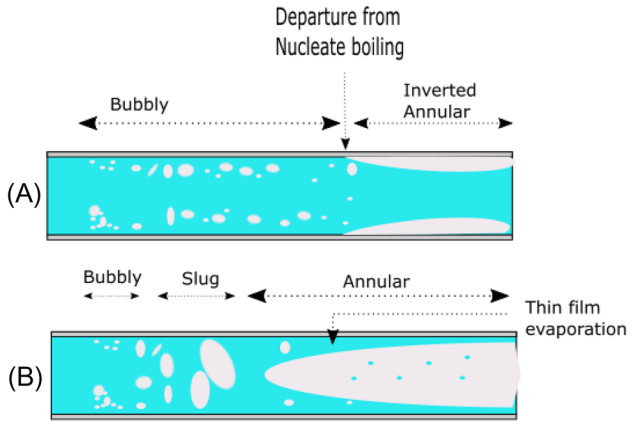

Fig. 7 Schematic representation of (**a**) liquid convection mechanism in subcooled flow boiling and (**b**) thin-film evaporation mechanism in saturated flow boiling

departure, coalescence, and generation frequency, which has yet to be explored.

3.5 Degree of superheat (T_{sup})

In a saturated boiling regime, the bulk fluid temperature is superheated (temperature is above the corresponding saturated temperature), and thin-film evaporation is the predominant heat transfer mechanism due to the bubble confinement. When the wall superheat is increased, the fluid is heated due to the increase in wall temperature, resulting in the formation of vapour bubbles. In the experimental investigation by Edel and Mukherjee (2011), for a local surface temperature of 100.9 °C, it took approximately 19 ms for a bubble to grow from 100 to 700 µm equivalent diameter. When the temperature was raised to 102.2 °C, it took approximately 13 ms to reach its maximum size. When it was further increased to 103.7 °C, it took only 9 ms for the bubble to reach its size, which demonstrates that the growth of the bubble varies linearly with wall superheat.

In addition, the thin layer around the vapour core expands as the superheat increases. This increased vapour generation pushes the upstream and downstream interfaces away from the bubble centre and towards the elongated thin-film regions. This elongated thin film increased the liquid–vapour interface's surface area, hence accelerating the bubble's growth. Compared to its initial linear growth, the bubble's growth rate becomes exponential after it approaches the diameter of the channel (Edel and Mukherjee 2011; Wong and Chong 2015). However, the expansion of the nucleating bubble prior to its departure impedes fluid movement in the microchannel. This blocking effect grows as the bubble expands and disappears when the bubble dissipates.

As the liquid superheated, it inhibits the growth of fluid flow in the microchannel, hence increasing flow resistance (Bogojevic et al. 2013; Dong et al. 2012). These bubbles are mainly affected by buoyancy, surface tension, and additional pressure during the quasi-static growth process, where the bubble contact line diameter expands first and then shrinks (Zhang et al. 2020; Yin et al. 2019). This suggests that HTC would be enhanced with mass flux at a higher saturation temperature and lower wall superheat (Markal et al. 2016b; Yan et al. 2019).

However, at high saturation temperatures, HTC is reduced due to a drop in the onset nucleate boiling temperature (Liao et al. 2019; Dalkılıç et al. 2020). Despite the fact that the bubble growth rate was linear with superheat, this growth rate caused pressure fluctuations and flow reversals after reaching the channel diameter. Table 5 shows key observations of both subcooled and superheated with parameter constraints in a microchannel.

3.6 Orientation/gravity effect

In the microscale, the surface tension force plays a dominant role compared to the gravity force. However, the CHF triggering mechanism depends on orientation factors, such as the upward-facing region, where buoyancy forces remove the vapour from the wall in a vertical direction. The vapour stratifies beneath the heated wall in the downwards facing region, resulting in a reduction in CHF values. These effects were complicated by the buoyancy force, which dominates at low velocities because of weak inertia. Increasing the liquid velocity imparts greater significance to the liquid inertia. In fact, high velocity can completely negate the effects of orientation, producing virtually equal CHF for both downward and upwards flow (Zhang et al. 2002). Krishnan et al. (2017) examined various orientations, including horizontal upward flow (HU), horizontal downward flow (HD), vertical upward flow (VUF), vertical downward flow (VDF), and horizontal with heating area vertically oriented (HV). The orientation on flow boiling was found to be negligible except for VDF orientation due to the commencement of earlier CHF. Individually, the bubbles nucleated at the nucleation sites evolved into vapour slugs (bubbles merging). Furthermore, rapid evaporation combined with frequent merging of nucleated bubbles and vapour slugs results in frequent churn flow. Even though backflow is common in all orientations, it is significantly more evident in the VDF orientation due to gravity-aided vapour backflow extending up to the inlet plenum, resulting in channel misdistribution. Also, Krishnan et al. (2017) and Suresh (2019) recommend the VUF for the microchannel flow boiling due to the buoyancy-assisted bubble movement helping to clear the channel before getting it clogged with vapour bubbles, reducing pressure drop and increasing CHF. However, in the consideration of the nucleate-dominant mechanism by Saisorn et al. (2018) with the HTC as a strong function of heat flux, the change in the

Table 5 Summary of subcooling and superheat with parameter constraints in microchannel flow boiling

Authors	Working fluid	Subcooling/superheat range	Parameter constraints	Key observation
Liao et al. (2019)	FC-72	T_{sat} = 35–50 °C	D_h = 60 µm, H = 100 µm, q = 0.67–4.5 W/cm^2 and G = 94–138 kg/m^2 s	ONB decreases with Sat. temp
Yan et al. (2019)	R134a	T_{sat} = 21.6–32.9 °C	D_h = 0.5 mm, 45 mm, q = 49.9–580.1 kW/m^2 and G = 132–1529 kg/m^2 s	HTC increases with Sat. temp
Markal et al. (2016b)	De-ionized water	Inlet temp. 50 ± 1 °C	29 Parallel square microchannels, D_h = 150 µm, G = 51, 64.5, 78 and 92.6 kg/m^2 s and q = 59.3—84.1 kW/m^2	HTC decreases with heat flux
Dalkılıç et al. (2020)	R134a	T_{sat} = 20–28 °C	D_h = 421 µm, 40 mm long microchannel, G = 1000 kg m^{-2} s^{-1} at x = 0.01–0.20 with q = 250 kW m^{-2}	CHF decreases with sat. temp
Qu and Mudawar (2002)	De-ionized water	Inlet temp. 30–90 °C	21 Rectangular 231 × 713 µm^2, liquid velocities 0.13–1.44 m/s, P_{out} = 1.2 bar	Incipient heat flux varies inversely with inlet temperature
Wojtan et al. (2006)	R-134a and R-245fa	Inlet temp. 2–15 °C	D_h = 0.5 and 0.8 mm, T_{sat} = 35 °C & q = 464—125 MW/m^2	Velocity as a strong dependence of CHF
Liu et al. (2005)	HFE-72000	Inlet temp. 50 ± 1 °C	275 × 636 µm^2	Functional dependence of HTC on subcooling
Saikia et al. (2019)	Water	T_{sub} = 0–16.9 °C	Pressure 5–17 bar and Q = 8.5–13.1 kW	The instability range varies with subcooling
Lee and Karayiannis (2020)	HFE-7200	T_{sub} = 5–20 K	20 mm × 20 mm, G = 200 kg/m^2 s, P = 1 bar, q = 25.9 and 180.7 kW/m^2	Flow oscillation is found to be delayed with subcooling
Ramesh et al. (2019)	Water	T_{sub} = 30–70 °C	1.0 mm wide × 0.49 mm deep, G = 528–1188 kg/m^2 s and q = 260–1100 kW/m^2	The incipient heat flux increases with inlet subcooling (decrease in inlet temp.) and HTC increases with fluid inlet temperature

flow pattern, the HTC and pressure drop yielded enhanced high heat transfer results for VDF with a higher pressure drop. The schematic of the microchannel heat exchanger at the different orientations is shown in Fig. 8.

According to Lavin et al. (2019), the influence of rotation (0°, 45°, and 60°) has no effect on the transition of the flow pattern, since the bubble shape varies from flat to spherical depending on the inclination. There is a distinction between the stratification effects, which were based on the asymmetry phase distribution of 45° and 60° channel rotation, and decreased flow velocity. At high mixing velocities, however, this difference disappears, demonstrating that it was mostly due to the higher effective height of the rotating test section. A few researchers also studied inclination effects, but the maximum increase in HTC seldom reaches 10% compared to the horizontal case (Gong et al. 2020; Vermaak et al. 2020; Vlachou and Karapantsios 2018). Due to the transition regime, the orientation effect had a significant impact on the HTC, notably between 45° and 60°. When the orientation angle is less than 45°, bubble departure from the heating surface is partially impeded by the wall due to buoyancy force, causing the main flow to be the dominant bubble motion. When the orientation angle was greater than 60°, the bubble motion was governed by the main flow and buoyancy forces, which will be significant for bubble motion at low flow rates.

Even though the channel inclination had a larger HTC than a horizontal or vertical surface, the influence was less than 10%, as discussed above. In addition, it was unfair to compare the results of horizontal and vertical configurations due to the inherent promotion of the annular flow regime. Also, difficulty in measuring due to the effect of gravity and the tendency for stratification to flow (O'Donovan and Grimes 2020; Liu et al. 2021). In the case of mini-gap or open microchannel heat sinks, it has been observed that orientation has no influence (Balasubramanian et al. 2018; Krishnan et al. 2018). The open manifold space over the microchannels allows bubble nucleation to continue within

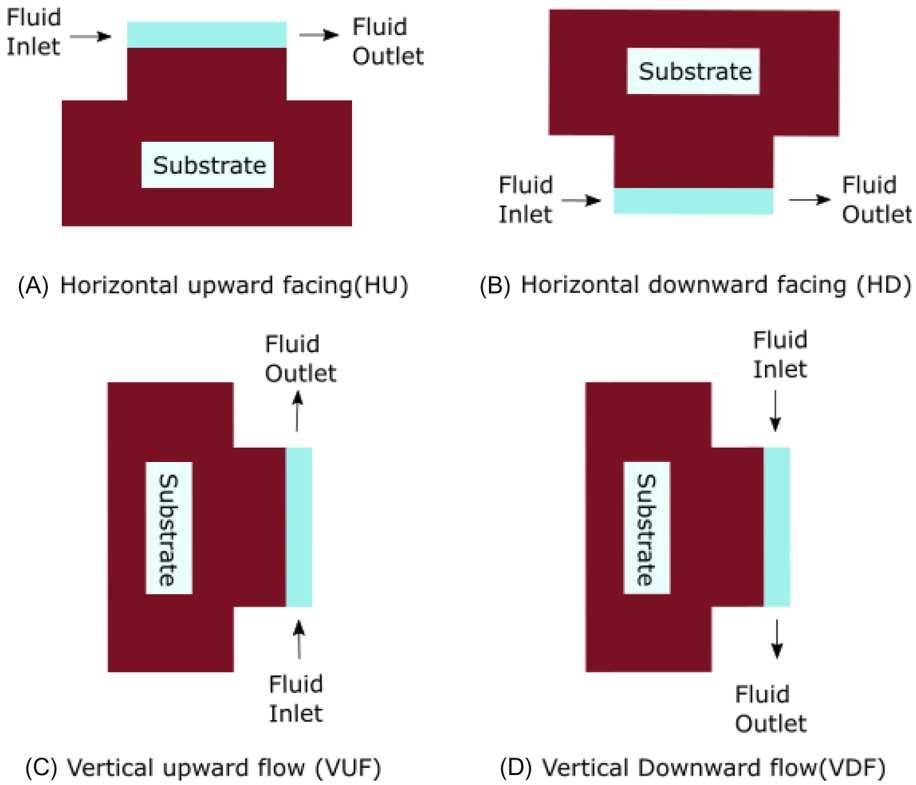

Fig. 8 Schematic of the different orientations of the microchannel heat sink

the channel even when the manifold region is occupied by vapour. Additionally, when the inertia and gravity force directions were opposite, the interaction between vapour bubbles was minimised. The flow behaviour based on orientation in various operational conditions is depicted in Table 6.

4 Thermophysical properties of the system

4.1 Vapour quality (*x*)

Vapour quality describes the boiling process from a liquid to a vapour state. If vapour quality (x) is 1, it indicates dry vapour, while 0 indicates liquid saturation. At low temperatures, the vapour quality was inadequate, which had no influence on HTC. However, when it comes to high temperatures, very few studies have examined the vapour quality range.

At the intense evaporation of flow boiling at high temperatures, a vapour slug fills the microchannel, where the liquid–vapour interface of this slug begins to perturbate and deform. This perturbation of the interface grows over time and produces a tiny bubble to be generated in the bulk fluid where the vapour quality plays the dominant factor. Many studies agree that the HTC will rise with vapour quality, but will eventually follow an inverse V-shaped pattern (Cheng and Xia 2017; Bertsch et al. 2008). The reverse flow and thermo-capillary instability occur when molecules exit the vapour phase and exert a recoil force on the liquid. As a result, vapour recoil instabilities are thought to be the cause of flow reversal, pressure, and temperature fluctuations (Barber et al. 2009).

The critical point of vapour quality, which separates the stable and unstable boiling regimes, was independent of other parameters such as fluid inlet temperature, heat flux, etc. (Wang and Cheng 2008). Stable boiling occurred in bubbly and elongated bubbly/slug flows where the vapour bubble was generated and pushed by the incoming subcooled liquid. The unstable boiling resulted from the expansion of the vapour slug upstream, which caused a fluctuation in temperature and pressure. The experimental analysis by Bertsch et al. (2009) likewise demonstrates the reduction of HTC as vapour quality increases.

In addition, the high vapour quality of the vapour slug formation pushes the liquid back to the source, resulting in reverse flow and an increase in surface temperature due to non-removal heat in constant heat flux (Brutin et al. 2003). Furthermore, the liquid film becomes thinner, leading to an annular regime with frequent dry-out, affecting the heat transfer and triggering flow fluctuations (Costa-Patry and Thome 2013). Although vapour quality is an operating parameter in HTC and flow instability, only a few HTC correlations take it into account.

Table 6 Summary on the impact of orientation in microchannel flow boiling

Authors	Working fluid	Gravity orientation/inclination	Parameter constraints	Suggested orientation
Krishnan et al. (2017)	De-ionized water	HU, HV, VUF and VDF	31 Parallel "U" shaped microchannels of 305 × 290 µm, flow rate 50–150 ml/min, Q 44.1–99.3 W/cm^2 and inlet temperature 35 °C	VUF for higher CHF and fewer pressure fluctuations
Saisorn et al. (2018)	R-134a	Horizontal flow, VUF and VDF	1 mm-Diameter channel, sat. pressure 8 bar, heat flux 1–60 kW/m^2, and mass flux 250–820 kg/m^2 s	VUF for cooling applications
Vlachou and Karapantsios (2018)	Water	0°, 30°, 45°, 60°, 90°, 120°, 150°	10 mm High, 40 mm wide and 120 mm long. mass flux: 330, 630, 830 kg/m^2 s; heat flux: 300–1000 kW/m^2	60° and 90° for higher heat fluxes
Balasubramanian et al. (2018)	De-ionized water	HU, HD, VUF and VDF	31 Parallel microchannels with 400 µm uniform gap with 305 × 312 µm having a fin thickness 300 µm with mass flux ranging from 77 to 911 kg/m^2 s	Orientation effect was negligible
Suresh (2019)	De-ionized water	HU, HD, VUF and VDF	D_h 100 µm, 300 µm, 500 µm and 1000 µm, mass flux: 100–900 kg/m^2 s	Negligible effects on 100, 300 µm with VUF as best orientation all channel
Krishnan et al. (2018)	De-ionized water	HU, HD, VUF and VDF	Hydraulic diameter (D_h) of 435 µm mass fluxes (G) ranging from 193 to 911 kg/m^2 s	Negligible effect of gravity
Lavin et al. (2019)	De-ionized water	− 90° to + 90° with channel axial rotations of 0, 45 and 60°	6.0 mm Deep, 6.5 mm wide, and 1.2 m long, mass velocities: 90–760 kg/m^2 s	Negligible effects of channel rotation
Gong et al. (2020)	De-ionized water	Orientations from 15° to 90°	Rectangular channel 17 mm × 10 mm, mass flow rates 110–288 kg/(m^2 s) and the qualities from 0.003 to 0.036	45°–60° affects transition regime
Vermaak et al. (2020)	FC-72	0° (heating from below) to 180° (heating from above)	High aspect ratio of 10 (5 mm × 0.5 mm) and hydraulic diameter of 909 µm, mass fluxes: 10, 20 and 40 kg/m^2 s at a sat. temperature of 56 °C	Bottom-heated cases (0° orientation) has 201% higher local heat transfer coefficients than other orientation

4.2 Contact angle (θ) and wettability

The term "wettability" refers to a fluid's ability to sustain contact with a solid surface due to intermolecular interactions. Higher wettability indicates hydrophilic surfaces (lower contact angle), and vice versa. The wetting state is dependent on the developed surface's chemical composition (intrinsic contact angle) and geometrical morphology (roughness ratio) (Yu et al. 2015). All practical surfaces exist with a small amount of irregularity that traps gases and necessitates a small amount of heat to trigger nucleation. It was termed Wenzel, Cassie, Hemi-wicking, or mixed state based on its wetness. Figure 9 depicts the schematic of contact angle and wettability.

Increasing the contact angle (hydrophobic surface) will increase vaporisation at the liquid–gas interface, resulting in an unstable nucleation due to the upstream superheated growth of large-diameter vapour bubbles (Liu et al. 2005; Li and Cheng 2004). Also, due to the larger nucleation site density, the unstable bubble results in cyclic temperature oscillations and a higher pressure drop in hydrophobic microchannels than in hydrophilic microchannels (Choi and Kim 2011; Kim and Lee 2019). However, in the mechanism of thin-film evaporation, the hydrophilic surface improved heat transfer in microchannel flow boiling. In contrast to nucleate boiling, the bubble had a short duration and a modest departure diameter (which improves heat transfer with the decrease in contact angle). The Reynolds number and the degree of subcooling can influence the contact angle, particularly when the bubble begins to grow (Sinha et al. 2019; Mukherjee 2009).

Katiyar et al. (2016) highlighted that when the contact angle increases, the length occupied by the bubble's base grows, resulting in a decrease in heat inflow from the bottom wall, leading to a slower bubble development rate. Larger bubbles are more successful at disrupting the thermal boundary layer that forms around them, resulting in an increase in heat transfer. When the bubbles have departed, it is a static condition, because the buoyancy and D_h esion forces are balanced. Otherwise, as the a D_h esive force between the hydrophobic surface and bubbles is greater, a greater buoyancy force is required to counteract it, resulting in a bigger bubble departure diameter than with the hydrophilic surface.

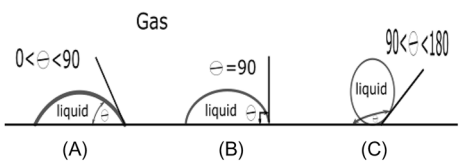

Fig. 9 Schematic drawing of contact angle and wettability; **a** wetting surface—hydrophilic, **b** non-wetting and **c** highly non-wetting—hydrophobic (Karayiannis and Mahmoud 2017)

In addition, hydrophilic surfaces with shorter bubble growth and bubble durations have superior heat transfer properties (Vontas et al. 2021; Sun et al. 2018), such that the "aged" channel has superior thermal performance over the "newly machined" channels, due to the repeated studies, the heating surface has become more thermally oxidised, making it easier to a D_h ere to Jayaramu et al. (2019).

Liu et al. (2011) investigated the effect of wettability on the super-hydrophilic surface (contact angle of less than 10°). Due to the super wetting surfaces, numerous small-diameter bubbles are generated with the decline in bubble departure size. The local dry-out occurred on untreated hydrophilic surfaces rather than the super-hydrophilic surface. The heat transfer performance was improved with super-hydrophilicity surfaces with the achievement of a zero-contact angle at high temperatures. However, the nucleation of a bubble on a super-hydrophilic surface is not readily obtained at low heat flux and high mass flux (Köhling and Wagner 2021; Zhou et al. 2017).

Betz et al. (2010, 2011, 2013), Dyke et al. (2015), and Wang et al. (2017) used a combination of biphilic surface patterns (pool boiling). The combined advantage of both hydrophobic (large bubble departure diameter and abundance of nucleation sites) and hydrophilic (smaller departure diameter, which prevents bubble merging). These combinations increased CHF and HTC due to increased nucleation sites and wettability, promoting bubble detachment and local dry-out (Hsu et al. 2021; Lin et al. 2021). Table 7 shows a summary of thermo-physical properties like the quality of the vapour, the contact angle, and the surface tension in microchannel flow boiling.

4.3 Surface tension (σ)

During the boiling process, vapour bubbles are generated at the bottom of the channel, and their departure to the surface is governed by two opposing forces: buoyancy (acting upwards) and surface tension (acting downward). The surface tension force originates from the contact angle fluctuations along the contact line caused by the influence of the liquid flow, which is dominant at the microscale due to the uniform production of slug flow and the avoidance of stratified flow (Kandlikar 2002, 2010). When the surface tension is decreased, bubble merging will be prevented or delayed, boosting the HTC by preserving the flow pattern, preventing coalescence, and producing tiny bubbles with a higher departure rate. In addition, the nucleation site density and bubble removal frequency rise with reduced bubble diameter, resulting in an increase in HTC, as depicted in Fig. 10 (Raza et al. 2016). However, higher surface tension causes a less severe, longer transition (Liu and Wang 2019). At high heat flux, the addition of a surfactant (a chemical that reduces liquid surface

Table 7 Selected literature on thermo-physical properties with parameter constraints

Authors	Working fluid	Geometry/surfactant	Parameter constraints	Optimum values
For critical vapour quality				
Barber et al. (2009)	De-ionized Water	D_h = 727 µm,	q = 4.26 kW/m^2, $G = 1.13 \times 10^{-5}$ kg/s	Influencing pressure and temperature fluctuation
Costa-Patry and Thome (2013)	R-134a, 236fa, 245fa and 1234ze (E)	D_h = 148 µm–3 mm	G = 569 kg m^{-2} s^{-1}, T_{sat} = 29.9 °C	Inverse V shape for HTC
Wang and Cheng (2008)	De-ionized water	D_h = 155 µm	Q_{eff} = 565–570 kW/m^2, G = 117.8 kg/m^2 s, and T_{in} = 20 °C	x_e = 0.013
Bertsch et al. (2009)	R-134a and R-245fa	D_h = 1.09 and 0.54 mm	T_{sat} = 8–30 °C, G = 20–350 kg m^{-2} s^{-1}, and q = 0–22 W cm^{-2}	x_e = 0.5
Bertsch et al. (2008)	HFC-134a	D_h = 1.09 mm and aspect ratio 2.5	G = 20.3—81 kg m^{-2} s^{-1} wall q = 0–20 W/cm^2	x_e = 0.2
Dalkılıç et al. (2020)	R134a	D_h = 421 µm	G = 1000 kg m^{-2} s^{-1}, q = 250 kW m^{-2}	HTC declines with x
For optimum surfactant				
Hetsroni et al. (2004)	Water	Non-ionic surfactant (alkyl glycosides)	m = 5.7 kg/m^2 s, q = 90–110 kW/m^2	4 Times increase in HTC
Klein et al. (2005)		APG	D = 4 mm, m = 0.042 kg/s, 145 kPa	Optimum conc. exists
Hetsroni et al. (2007)		Alkyl (8–16)	G = 5–18 kg/m^2 s and q = 40–200 kW/m^2	Optimum ppm: 300
Yang et al. (2019)		Glycerol	D_h = 200 µm, T = 50 °C and Q = 10–30 kW/m^2	Optimum V_f. 5%
Wang and Li (2017)		Cetyltrimethyl ammonium chloride (CTAC) with the addition of sodium salicylate (NaSal)	G = 192–406 ml/min, T_{in} = 80 °C and P_{out} = 101.3 kPa	Optimum ppm: 100
Wang et al. (2019)			6.0 mm × 3.5 mm and length 300 mm	Boiling without bubbles merging has a higher and more stable average Nu number
Contact angle and wettability				
Li and Cheng (2004)	Water	–	P = 8.72 MPa, G: 0–6 mg/s and q: 250–350 W/cm^2	Larger contact angle will reduce the nucleation temperature
Mukherjee (2009)	Water	–	T_{sup} = 8 K	Heat transfer improved with decrease in contact angle
Sinha et al. (2019)	Water	D_h = 6.67 mm	Re = 2400–7200 and ΔT_{sub} = 2.5—8.5 °C	Contact angle reduced with Re and subcooling
Siddique et al. (2020)	Water, FC72, R113 and R245fa	229 µm × 229 µm × 916 µm	T_{sup} = 2.1 °C, G = 90 kg s^{-1} m^{-2}	Decrease in latent heat and density ratio increase the bubble growth and Nu.no
Vontas et al. (2021)	DI-water	D_h = 200 µm and length 2.4 mm	q = 20, 50 and 100 kW/m^2 and G = 74, 150 and 295 kg/m^2 s	Bubble departure was faster in hydrophilicity
Sun et al. (2018)	DI-water	–	Numerical simulation through LBM	Hydrophilic surface have better heat transfer than hydrophobic
Köhling and Wagner (2021)	DI-water	–	Re = 0.5, We = 10^{-4}, T = 110 °C	At high temp. super-hydrophilic surface can reach zero-contact angle
Liu et al. (2011)	DI-water	105 × 1000 × 30,000 µm	q = 230–354.9 kW/m^2 and G = 50–583 kg/m^2 s	Steady boiling in hydrophilic and unsteady nucleation in hydrophobic

Table 7 (continued)

Authors	Working fluid	Geometry/surfactant	Parameter constraints	Optimum values
Choi and Kim (2011)	Water–liquid and Nitrogen–gas	D_h = 141, 143, 304, 322 and 490 µm	G: 66–1000 kg/m^2 s	HTC and pressure drop was higher for hydrophobic than hydrophilic microch
Zhou et al. (2017)	De-ionized water	–	G = 120–360 kg/m^2 s, q = 4–20 W/cm^2 with x = 0.03–0.1	Constant heat transfer in super-hydrophilic surface
Kim and Lee (2019)	De-ionized water	–	q = 20–500 kg/m^2 s	Hydrophilic and hydrophobic channels enhanced the CHF at low and high mass fluxes, respectively

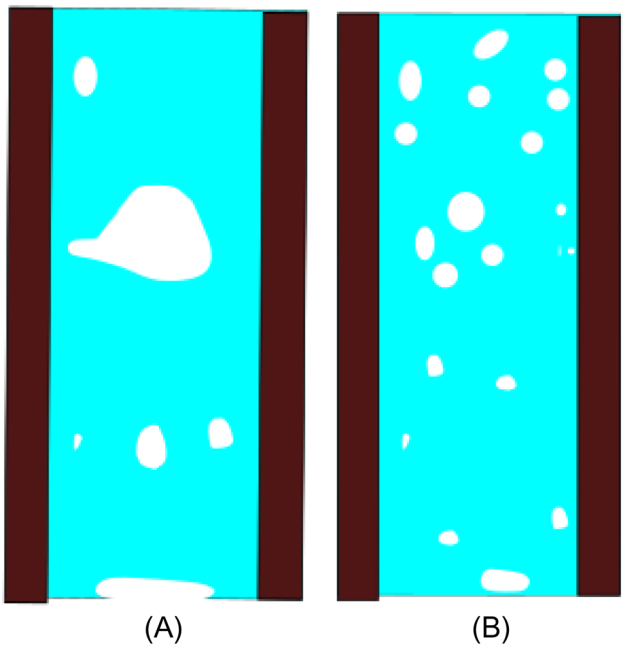

Fig. 10 Flow boiling in **a** water at 290 KW/m^2 at 5.5 ms and **b** 100 ppm CTAC/NaSal solution at 290 KW/m^2 at 60 ms (Wang et al. 2019)

tension) causes the formation of a nucleus containing a lot of tiny bubbles, which tends to cover the entire heater surface with a vapour blanket. Compared to water, more active nucleation sites increase HTC as heat flux increases (Hetsroni et al. 2004).

The influence of surface tension is neither straightforward nor direct, as it increases the early ONB by lowering the surface tension and dynamic contact angle of water. All surfactants have an optimal range for increasing heat removal (Klein et al. 2005; Hetsroni et al. 2007). The thermal performance will deteriorate when more surfactant is used. This drop in HTC is a result of widespread coverage of the Benard–Marangoni effect (Yang et al. 2019). Nonetheless, the concentration gradient stimulates flow, which in turn induces the temperature gradient in the same direction.

On optimum surfactant, mass transfer will occur between the sublayer and bulk layer and vice versa. Both heat transfer and mass transfer will be balanced as a result. With excessive mass concentration, however, the mixture's density increases, impeding mass transmission from the sublayer to the main layer. This results in resistance, which necessitates greater thermal energy to overcome. The HTC decreases when the bulk concentration of surfactant exceeds a particular threshold. Similarly, the CHF was increased by the addition of surfactant, but remained unchanged at higher concentrations.

As demonstrated in Fig. 10, when compared to water, the bubble in the surfactant solution has a small-diameter and a long-period without merging. These bubbles increased flow velocity and amplified disturbances, facilitating heat transfer and producing greater pressure variations (Wang and Li 2017; Wang et al. 2019). Cumulatively, we discover that bubble merging is the process that reduces the efficiency of heat transfer, particularly in the middle flow. Another factor of surfactant addition that enhances boiling heat transfer is preventing bubble merging and delaying early dry-out.

5 Conclusion

This review paper is primed to present the most recent hypothesis on the physical properties of microchannel flow boiling. Although numerous studies have been conducted in the last 2 decades, there is no agreed upon dominant mechanism. It appears that the nucleate, convective, and thin-film evaporative mechanisms are contributing significantly and simultaneously to the heat transfer process of microchannel flow boiling. It was difficult to segregate the contributions of each mechanism. Below is a summary of each parameter's contribution to microchannel flow boiling heat transfer.

- In comparison to flow properties, the design parameters, namely aspect ratio and channel arrangement, play a crucial effect in the boiling process. Complex configurations and higher aspect ratio channels result

in a higher HTC (breaking the thermal boundary layer) with a pressure drop penalty and difficult-to-decode bubble dynamics.

- Higher mass flux enhanced incipient heat flux by delaying nucleation frequency, resulting in a convective boiling mechanism. Increased heat flux, on the other hand, accelerated early nucleation and flow pattern transition, resulting in a nucleate-dominated mechanism.
- Subcooling acts as a function of velocity and functional dependence of heat flux. With an increase in subcooling, the stability of the flow was increased due to a delay in slug flow and bubble generation. Liquid convection plays a crucial role in the sub-cooled heat transfer mechanism.
- At high saturated flow boiling conditions, the thin film at the end of the annular plays an important role in heat transfer.
- The vapour quality is said to enhance the HTC up to the point where a thin film exists. But beyond thin film, it declines the HTC due to dry-out.
- Friction pressure plays the dominant role, which can also influence independent variables like vapour density, surface tension, latent heat, etc. The bubble growth and diameter, which influence the HTC, vary inversely with pressure. However, increased pressure stabilises the system.
- Though gravity/orientation effects are negligible in the microchannel due to its dominant surface tension effects. The VUF acts as a suitable orientation for electronics cooling.
- The hydrophilic surface enhanced the heat transfer with a smaller contact angle. A hydrophobic surface generates flow oscillation because of unstable bubbles with a greater nucleation density.
- By reducing the surface tension, bubble merging is prevented, enhancing the HTC up to the optimum concentration of surfactant. On further increases, it becomes ineffective due to the Benard–Marangoni effect.
- Observed discrepancies in the behaviour of flow boiling indicate that the analogy of heat transfer in the macro-channel cannot be transferred to the microchannel due to the differences in the behaviour of flow boiling as observed. And it is difficult to determine the generalised micro-channel flow boiling mechanism from the available literature specific to their experimental data. To design and optimise microchannel flow boiling, it is necessary to investigate the flow boiling qualities and bubble behaviour in the microchannel at various operating ranges.

Declarations

Conflict of interest The authors declare that they have no conflict of interest.

References

Abdous MA, Holagh SG, Shamsaiee M, Saffari H (2019) The prediction of bubble departure and lift-off radii in vertical U-shaped channel under subcooled flow boiling based on forces balance analysis. Int J Therm Sci 142:316–331

Ajith Krishnan R, Balasubramanian KR, Suresh S (2018) Experimental investigation of the effect of heat sink orientation on subcooled flow boiling performance in a rectangular microgap channel. Int J Heat Mass Transf 120:1341–1357. https://doi.org/10.1016/j.ijheatmasstransfer.2017.12.133

Ali R, Palm B, Maqbool MH (2012) Flow boiling heat transfer of refrigerants R134a and R245fa in a horizontal micro-channel. Exp Heat Transf 25(3):181–196

Al-Neama AF, Kapur N, Summers J, Thompson HM (2017) An experimental and numerical investigation of the use of liquid flow in serpentine microchannels for microelectronics cooling. Appl Therm Eng 116:709–723

Al-Zaidi AH, Mahmoud MM, Karayiannis TG (2021) Effect of aspect ratio on flow boiling characteristics in microchannels. Int J Heat Mass Transf 164:120587

Anwar Z, Palm B, Khodabandeh R (2014) Flow boiling heat transfer and dryout characteristics of R152a in a vertical mini-channel. Exp Therm Fluid Sci 53:207–217

Balasubramanian K, Jagirdar M, Lee PS, Teo CJ, Chou SK (2013) Experimental investigation of flow boiling heat transfer and instabilities in straight microchannels. Int J Heat Mass Transf 66:655–671

Balasubramanian KR, Krishnan RA, Suresh S (2018) Spatial orientation effects on flow boiling performances in open microchannels heat sink configuration under a wide range of mass fluxes. Exp Therm Fluid Sci 99:392–406

Bao ZY, Fletcher DF, Haynes BS (2000) Flow boiling heat transfer of Freon R11 and HCFC123 in narrow passages. Int J Heat Mass Transf 43(18):3347–3358

Barber J, Sefiane K, Brutin D, Tadrist L (2009) Hydrodynamics and heat transfer during flow boiling instabilities in a single microchannel. Appl Therm Eng 29(7):1299–1308

Barber J, Brutin D, Sefiane K, Tadrist L (2010) Bubble confinement in flow boiling of FC-72 in a 'rectangular' microchannel of high aspect ratio. Exp Therm Fluid Sci 34(8):1375–1388

Basu N, Warrier GR, Dhir VK (2002) Onset of nucleate boiling and active nucleation site density during subcooled flow boiling. J Heat Transf 124(4):717–728

Basu S, Ndao S, Michna GJ, Peles Y, Jensen MK (2011) Flow boiling of R134a in circular microtubes—part I: study of heat transfer characteristics. J Heat Transf 133(5):051502

Bertsch SS, Groll EA, Garimella SV (2008) Refrigerant flow boiling heat transfer in parallel microchannels as a function of local vapor quality. Int J Heat Mass Transf 51(19–20):4775–4787

Bertsch SS, Groll EA, Garimella SV (2009) Effects of heat flux, mass flux, vapor quality, and saturation temperature on flow boiling heat transfer in microchannels. Int J Multiph Flow 35(2):142–154

Betz AR, Attinger D (2010) Can segmented flow enhance heat transfer in microchannel heat sinks? Int J Heat Mass Transf 53(19–20):3683–3691

Betz AR, Xu J, Qiu H, Attinger D (2010) Do surfaces with mixed hydrophilic and hydrophobic areas enhance pool boiling? Appl Phys Lett 97(14):141909

Betz AR, Jenkins J, Attinger D (2013) Boiling heat transfer on superhydrophilic, superhydrophobic, and superbiphilic surfaces. Int J Heat Mass Transf 57(2):733–741

Betz AR, Jenkins JR, Kim C-J, Attinger D (2011) Significant boiling enhancement with surfaces combining superhydrophilic and superhydrophobic patterns. In: 2011 IEEE 24th international conference on micro electro mechanical systems, pp 1193–1196

Bhandari P, Prajapati YK (2021) Thermal performance of open microchannel heat sink with variable pin fin height. Int J Therm Sci 159:106609

Bhuvankar P, Dabiri S (2020) Simulation of flow boiling in microchannels: effects of inlet flow rate and hot-spots. Int J Heat Fluid Flow 85:108616

Bigham S, Moghaddam S (2015) Microscale study of mechanisms of heat transfer during flow boiling in a microchannel. Int J Heat Mass Transf 88:111–121

Bogojevic D, Sefiane K, Walton AJ, Lin H, Cummins G (2009) Two-phase flow instabilities in a silicon microchannels heat sink. Int J Heat Fluid Flow 30(5):854–867

Bogojevic D et al (2011) Experimental investigation of non-uniform heating effect on flow boiling instabilities in a microchannel-based heat sink. Int J Therm Sci 50(3):309–324

Bogojevic D, Sefiane K, Duursma G, Walton AJ (2013) Bubble dynamics and flow boiling instabilities in microchannels. Int J Heat Mass Transf 58(1–2):663–675

Boye H, Staate Y, Schmidt J (2007) Experimental investigation and modelling of heat transfer during convective boiling in a minichannel. Int J Heat Mass Transf 50(1–2):208–215

Brutin D, Topin F, Tadrist L (2003) Experimental study of unsteady convective boiling in heated minichannels. Int J Heat Mass Transf 46(16):2957–2965

Celata GP, Cumo M, Dossevi D, Jilisen RTM, Saha SK, Zummo G (2012) Flow pattern analysis of flow boiling inside a 0.48 mm microtube. Int J Therm Sci 58:1–8

Chen L, Tian YS, Karayiannis TG (2006) The effect of tube diameter on vertical two-phase flow regimes in small tubes. Int J Heat Mass Transf 49(21–22):4220–4230

Chen CA, Lin TF, Ali HM, Amani P, Yan W-M (2019) Bubble dynamics in evaporation flow of R-134a in narrow annular ducts due to flow rate oscillation. Int Commun Heat Mass Transf 100:27–34

Cheng L, Xia G (2017) Fundamental issues, mechanisms and models of flow boiling heat transfer in microscale channels. Int J Heat Mass Transf 108:97–127

Cheng KX, Foo ZH, Ooi KT (2020) Heat transfer enhancement through periodic flow area variations in microchannels. Int Commun Heat Mass Transf 111:104456

Cheng X, Yao Y, Wu H (2021) An experimental investigation of flow boiling characteristics in silicon-based groove-wall microchannels with different structural parameters. Int J Heat Mass Transf 168:120843

Choi C, Kim M (2011) Flow pattern based correlations of two-phase pressure drop in rectangular microchannels. Int J Heat Fluid Flow 32(6):1199–1207

Chung P-Y, Kawaji M (2004) The effect of channel diameter on adiabatic two-phase flow characteristics in microchannels. Int J Multiph Flow 30(7–8):735–761

Collier JG, Thome JR (1994) Convective boiling and condensation. Clarendon Press, Oxford

Costa-Patry E, Thome JR (2013) Flow pattern-based flow boiling heat transfer model for microchannels. Int J Refrig 36(2):414–420

Dalkılıç AS, Celen A, Erdoğan M, Sakamatapan K, Newaz KS, Wongwises S (2020) Effect of saturation temperature and vapor quality on the boiling heat transfer and critical heat flux in a microchannel. Int Commun Heat Mass Transf 117:104768

Dario ER, Passos JC, Simón MLS, Tadrist L (2016) Pressure drop during flow boiling inside parallel microchannels. Int J Refrig 72:111–123

Deng D, Chen R, He H, Feng J, Tang Y, Zhou W (2015) Effects of channel dimension, heat flux, and mass flux on flow boiling regimes in microchannels. Exp Therm Fluid Sci 64:13–22. https://doi.org/10.1016/j.expthermflusci.2015.01.015

Diaz MC, Schmidt J (2007) Experimental investigation of transient boiling heat transfer in microchannels. Int J Heat Fluid Flow 28(1):95–102

Dong Z, Xu J, Jiang F, Liu P (2012) Numerical study of vapor bubble effect on flow and heat transfer in microchannel. Int J Therm Sci 54:22–32

Edel ZJ, Mukherjee A (2011) Experimental investigation of vapor bubble growth during flow boiling in a microchannel. Int J Multiph Flow 37(10):1257–1265

Farahani SD, Karami M (2019) Experimental estimation of local heat flux on boiling surface in a mini-channel. Int Commun Heat Mass Transf 108:104271

Ghiaasiaan SM, Chedester RC (2002) Boiling incipience in microchannels. Int J Heat Mass Transf 45(23):4599–4606

Ghosh S, Das AK, Vaidya AA, Mishra SC, Das PK (2012) Numerical study of dynamics of bubbles using lattice Boltzmann method. Ind Eng Chem Res 51(18):6364–6376

Gong S, Mei Y, Amin MY, Zhang B, Ma W (2020) Orientation effect on heat transfer coefficient of a downward surface for flow boiling in a rectangular channel under low flow rate. Int J Heat Mass Transf 153:119594

Harirchian T, Garimella SV (2009a) Effects of channel dimension, heat flux, and mass flux on flow boiling regimes in microchannels. Int J Multiph Flow 35(4):349–362

Harirchian T, Garimella SV (2009b) The critical role of channel cross-sectional area in microchannel flow boiling heat transfer. Int J Multiph Flow 35(10):904–913

Hedau G, Dey P, Raj R, Saha SK (2020) Experimental and numerical investigation of the effect of number of parallel microchannels on flow boiling heat transfer. Int J Heat Mass Transf 158:119973

Hetsroni G, Zakin JL, Gurevich M, Mosyak A, Pogrebnyak E, Rozenblit R (2004) Saturated flow boiling heat transfer of environmentally acceptable surfactants. Int J Multiph Flow 30(7–8):717–734

Hetsroni G, Gurevich M, Mosyak A, Rozenblit R (2007) Effect of surfactant concentration on saturated flow boiling in vertical narrow annular channels. Int J Multiph Flow 33(11):1141–1152

Hsieh YY, Chiang LJ, Lin TF (2002) Subcooled flow boiling heat transfer of R-134a and the associated bubble characteristics in a vertical plate heat exchanger. Int J Heat Mass Transf 45(9):1791–1806

Hsu W-T, Lee D, Lee N, Yun M, Cho HH (2021) Enhancement of flow boiling heat transfer using heterogeneous wettability patterned surfaces with varying inter-spacing. Int J Heat Mass Transf 164:120596

Huang H, Thome JR (2017) An experimental study on flow boiling pressure drop in multi-microchannel evaporators with different refrigerants. Exp Therm Fluid Sci 80:391–407

Huh C, Kim MH (2006) An experimental investigation of flow boiling in an asymmetrically heated rectangular microchannel. Exp Therm Fluid Sci 30(8):775–784

Huh C, Kim MH (2013) Periodic flow boiling in a non-uniformly heated microchannel heat sink. Int J Heat Fluid Flow 42:164–175

In S, Jeong S (2009) Flow boiling heat transfer characteristics of R123 and R134a in a micro-channel. Int J Multiph Flow 35(11):987–1000

Jagirdar M, Lee PS (2020) Quasi-steady and transient study of heat transfer during sub-cooled flow boiling in a small aspect ratio microchannel. Int J Multiph Flow 133:103446

Jayaramu P, Gedupudi S, Das SK (2019) Influence of heating surface characteristics on flow boiling in a copper microchannel: experimental investigation and assessment of correlations. Int J Heat Mass Transf 128:290–318

Jiang Z et al (2019) Experimental study on the flow boiling oscillation characteristics in a rectangular multiple micro-channel. Exp Therm Fluid Sci 109:109902

Kandlikar SG (2002) Fundamental issues related to flow boiling in minichannels and microchannels. Exp Therm Fluid Sci 26(2–4):389–407

Kandlikar SG (2004) Heat transfer mechanisms during flow boiling in microchannels. J Heat Transf 126(1):8–16

Kandlikar SG (2005) High flux heat removal with microchannels—a roadmap of challenges and opportunities. Heat Transf Eng 26(8):5–14

Kandlikar SG (2010) Scale effects on flow boiling heat transfer in microchannels: a fundamental perspective. Int J Therm Sci 49(7):1073–1085

Kandlikar S, Garimella S, Li D, Colin S, King MR (2005) Heat transfer and fluid flow in minichannels and microchannels. Elsevier, Amsterdam

Karayiannis TG, Mahmoud MM (2017) Flow boiling in microchannels: fundamentals and applications. Appl Therm Eng 115:1372–1397

Katiyar G, Karagadde S, Saha SK, Sharma A (2016) Numerical modelling of bubble growth in microchannel using level set method. Int J Heat Mass Transf 101:719–732

Keepaiboon C, Thiangtham P, Mahian O, Dalkılıç AS, Wongwises S (2016) Pressure drop characteristics of R134a during flow boiling in a single rectangular micro-channel. Int Commun Heat Mass Transf 71:245–253

Kim J, Lee JS (2019) Numerical study on the effects of inertia and wettability on subcooled flow boiling in microchannels. Appl Therm Eng 152:175–183

Kingston TA, Weibel JA, Garimella SV (2018) High-frequency thermal-fluidic characterization of dynamic microchannel flow boiling instabilities: Part 1–Rapid-bubble-growth instability at the onset of boiling. Int J Multiph Flow 106:179–188

Klein D, Hetsroni G, Mosyak A (2005) Heat transfer characteristics of water and APG surfactant solution in a micro-channel heat sink. Int J Multiph Flow 31(4):393–415

Köhling J, Wagner V (2021) High speed picoliter droplet top-view analysis for advancing and receding contact angles, boiling regimes and droplet-droplet interaction. Int J Heat Mass Transf 169:120939. https://doi.org/10.1016/j.ijheatmasstransfer.2021.120939

Kong L, Liu Z, Jia L, Lv M, Liu Y (2020) Experimental study on flow and heat transfer characteristics at onset of nucleate boiling in micro pin fin heat sinks. Exp Therm Fluid Sci 115:109946

Krishnan RA, Balasubramanian KR, Suresh S (2017) The effect of heating area orientation on flow boiling performance in microchannels heat sink under subcooled condition. Int J Heat Mass Transf 110:276–293

Krishnan RA, Balasubramanian KR, Suresh S (2018) Experimental investigation of the effect of heat sink orientation on subcooled flow boiling performance in a rectangular microgap channel. Int J Heat Mass Transf 120:1341–1357

Kuo C-J, Peles Y (2009) Pressure effects on flow boiling instabilities in parallel microchannels. Int J Heat Mass Transf 52(1–2):271–280

Kwon B, Maniscalco NI, Jacobi AM, King WP (2019) High power density two-phase cooling in microchannel heat exchangers. Appl Therm Eng 148:1271–1277

Lavin FL, Kanizawa FT, Ribatski G (2019) Analyses of the effects of channel inclination and rotation on two-phase flow characteristics and pressure drop in a rectangular channel. Exp Therm Fluid Sci 109:109850

Lee VYS, Karayiannis TG (2020) Effect of inlet subcooling on flow boiling in microchannels. Appl Therm Eng 181:115966

Li J, Cheng P (2004) Bubble cavitation in a microchannel. Int J Heat Mass Transf 47(12–13):2689–2698

Li H, Hrnjak P (2017) Effect of periodic reverse flow on the heat transfer performance of microchannel evaporators. Int J Refrig 84:309–320

Li X, Jia L, Dang C, An Z, Huang Q (2018a) Effect of flow instability on flow boiling friction pressure drop in parallel micro-channels. Int Commun Heat Mass Transf 97:64–71

Li W, Zhou K, Li J, Feng Z, Zhu H (2018b) Effects of heat flux, mass flux and two-phase inlet quality on flow boiling in a vertical superhydrophilic microchannel. Int J Heat Mass Transf 119:601–613. https://doi.org/10.1016/j.ijheatmasstransfer.2017.11.145

Liao W-R, Chien L-H, Ghalambaz M, Yan W-M (2019) Experimental study of boiling heat transfer in a microchannel with nucleated-shape columnar micro-pin-fins. Int Commun Heat Mass Transf 108:104277

Lin S, Kew PA, Cornwell K (2001) Flow boiling of refrigerant R141B in small tubes. Chem Eng Res Des 79(4):417–424

Lin PH, Fu BR, Pan C (2011) Critical heat flux on flow boiling of methanol–water mixtures in a diverging microchannel with artificial cavities. Int J Heat Mass Transf 54(15):3156–3166. https://doi.org/10.1016/j.ijheatmasstransfer.2011.04.016

Lin Y, Luo Y, Li J, Li W (2021) Heat transfer, pressure drop and flow patterns of flow boiling on heterogeneous wetting surface in a vertical narrow microchannel. Int J Heat Mass Transf 172:121158

Ling K, Son G, Sun D-L, Tao W-Q (2015) Three dimensional numerical simulation on bubble growth and merger in microchannel boiling flow. Int J Therm Sci 98:135–147

Ling W, Zhou W, Yu W, Guo Z, Chen J (2019) Effects of operation parameters on thermal and hydraulic performances of a novel interlaced microchannel. Appl Therm Eng 147:143–154

Liu Q, Wang C (2019) Bubble interaction of annular flow in microchannel boiling. Int Commun Heat Mass Transf 101:76–81

Liu D, Lee P-S, Garimella SV (2005) Prediction of the onset of nucleate boiling in microchannel flow. Int J Heat Mass Transf 48(25–26):5134–5149

Liu TY, Li PL, Liu CW, Gau C (2011) Boiling flow characteristics in microchannels with very hydrophobic surface to super-hydrophilic surface. Int J Heat Mass Transf 54(1–3):126–134

Liu B et al (2021) Analysis of the critical heat flux of subcooled flow boiling in microgravity. Exp Therm Fluid Sci 120:110238

Loganathan R, Mohiuddin A, Gedupudi S (2020) Experimental investigation of the effect of bypass inlet on flow boiling in a mini/micro-channel. Int Commun Heat Mass Transf 110:104405

Luo Y et al (2020a) Three-dimensional numerical simulation of saturated annular flow boiling in a narrow rectangular microchannel. Int J Heat Mass Transf 149:119246

Luo Y, Zhang J, Li W (2020b) A comparative numerical study on two-phase boiling fluid flow and heat transfer in the microchannel heat sink with different manifold arrangements. Int J Heat Mass Transf 156:119864

Ma DD, Xia GD, Zong LX, Jia YT, Tang YX, Zhi RP (2019) Experimental investigation of flow boiling heat transfer performance in zigzag microchannel heat sink for electronic cooling devices. Int J Therm Sci 145:106003

Magnini M, Thome JR (2016) A CFD study of the parameters influencing heat transfer in microchannel slug flow boiling. Int J Therm Sci 110:119–136

Mahesh P, Kiran Kumar K, Balasubramanian K, Chandramohan VP, Lee PS, Chee Kong C (2021) Heat transfer enhancement using double taper microchannel. Proc Inst Mech Eng Part E J Process Mech Eng 236:975–990

Mahmoud MM, Kenning DBR, Karayiannis TG (2009) Single and two phase heat transfer and pressure drop in a 0.52 mm vertical metallic tube. In: 7th international conference on enhanced, compact and ultra-compact heat exchangers: from microscale phenomena to industrial applications, Heredia, Costa Rica, pp 13–18

Mamidi NK, Balasubramanian K, Kumar Kupireddi K, Chandramohan VP, Lee PS, Kong CC (2021) Heat transfer augmentation in a radial curved microchannel. Proc Inst Mech Eng Part E J Process Mech Eng 236:281–297

Markal B, Aydin O, Avci M (2016a) Effect of aspect ratio on saturated flow boiling in microchannels. Int J Heat Mass Transf 93:130–143

Markal B, Aydin O, Avci M (2016b) An experimental investigation of saturated flow boiling heat transfer and pressure drop in square microchannels. Int J Refrig 65:1–11

Mathew J, Lee P-S, Wu T, Yap CR (2019) Experimental study of flow boiling in a hybrid microchannel-microgap heat sink. Int J Heat Mass Transf 135:1167–1191

Mathew J, Lee P-S, Wu T, Yap CR (2020) Comparative study of the flow boiling performance of the hybrid microchannel-microgap heat sink with conventional straight microchannel and microgap heat sinks. Int J Heat Mass Transf 156:119812

McNeil DA, Raeisi AH, Kew PA, Hamed RS (2013) Flow boiling heat-transfer in micro to macro transition flows. Int J Heat Mass Transf 65:289–307

Mohiuddin A, Loganathan R, Gedupudi S (2020) Experimental investigation of flow boiling in rectangular mini/micro-channels of different aspect ratios without and with vapour venting membrane. Appl Therm Eng 168:114837

Mortada S, Zoughaib A, Arzano-Daurelle C, Clodic D (2012) Boiling heat transfer and pressure drop of R-134a and R-1234yf in minichannels for low mass fluxes. Int J Refrig 35(4):962–973

Mukherjee A (2009) Contribution of thin-film evaporation during flow boiling inside microchannels. Int J Therm Sci 48(11):2025–2035

Mukherjee A, Kandlikar SG (2009) The effect of inlet constriction on bubble growth during flow boiling in microchannels. Int J Heat Mass Transf 52(21–22):5204–5212

Naqiuddin NH et al (2018) Numerical investigation for optimizing segmented micro-channel heat sink by Taguchi–Grey method. Appl Energy 222:437–450

O'Donovan A, Grimes R (2020) Two-phase flow regime identification through local temperature mapping. Exp Therm Fluid Sci 115:110077

Park K, Noh K-J, Lee K-S (2003) Transport phenomena in the thin-film region of a micro-channel. Int J Heat Mass Transf 46(13):2381–2388

Prajapati YK, Pathak M, Khan MK (2015) A comparative study of flow boiling heat transfer in three different configurations of microchannels. Int J Heat Mass Transf 85:711–722

Prajapati YK, Pathak M, Khan MK (2017a) Bubble dynamics and flow boiling characteristics in three different microchannel configurations. Int J Therm Sci 112:371–382

Prajapati YK, Pathak M, Khan MK (2017b) Numerical investigation of subcooled flow boiling in segmented finned microchannels. Int Commun Heat Mass Transf 86:215–221

Qu W, Mudawar I (2002) Prediction and measurement of incipient boiling heat flux in micro-channel heat sinks. Int J Heat Mass Transf 45(19):3933–3945

Qu W, Mudawar I (2003) Flow boiling heat transfer in two-phase micro-channel heat sinks—I. Experimental investigation and assessment of correlation methods. Int J Heat Mass Transf 46(15):2755–2771

Raj S, Pathak M, Khan MK (2019) Effects of flow loop components in suppressing flow boiling instabilities in microchannel heat sinks. Int J Heat Mass Transf 141:1238–1251

Ramesh B, Jayaramu P, Gedupudi S (2019) Subcooled flow boiling of water in a copper microchannel: experimental investigation and assessment of predictive methods. Int Commun Heat Mass Transf 103:24–30

Raza MQ, Kumar N, Raj R (2016) Surfactants for bubble removal against buoyancy. Sci Rep 6(1):1–9

Revellin R, Thome JR (2007) Experimental investigation of R-134a and R-245fa two-phase flow in microchannels for different flow conditions. Int J Heat Fluid Flow 28(1):63–71

Sahar AM, Wissink J, Mahmoud MM, Karayiannis TG, Ishak MSA (2017) Effect of hydraulic diameter and aspect ratio on single phase flow and heat transfer in a rectangular microchannel. Appl Therm Eng 115:793–814

Saikia K, Pandey M, Basu DN (2019) Numerical investigation of the effect of inlet subcooling on flow instabilities in a parallel channel natural circulation boiling system. Prog Nucl Energy 114:13–21

Saisorn S, Wongpromma P, Wongwises S (2018) The difference in flow pattern, heat transfer and pressure drop characteristics of minichannel flow boiling in horizontal and vertical orientations. Int J Multiph Flow 101:97–112

Siddique A, Gb A, Agrawal A, Saha SK, Sharma A (2020) Study of bubble growth and microchannel flow boiling heat transfer characteristics using dynamic contact angle model. Therm Sci Eng Prog 20:100743. https://doi.org/10.1016/j.tsep.2020.100743

Singh SG, Kulkarni A, Duttagupta SP, Puranik BP, Agrawal A (2008) Impact of aspect ratio on flow boiling of water in rectangular microchannels. Exp Therm Fluid Sci 33(1):153–160

Sinha GK, Mahimkar S, Srivastava A (2019) Schlieren-based simultaneous mapping of bubble dynamics and temperature gradients in nucleate flow boiling regime: effect of flow rates and degree of subcooling. Exp Therm Fluid Sci 104:238–257

Sun T (2019) A numerical study on dynamics behaviors of multi bubbles merger during nucleate boiling by lattice Boltzmann method. Int J Multiph Flow 118:128–140

Sun T, Gui N, Yang X, Tu J, Jiang S (2018) Effect of contact angle on flow boiling in vertical ducts: a pseudo-potential MRT-thermal LB coupled study. Int J Heat Mass Transf 121:1229–1233. https://doi.org/10.1016/j.ijheatmasstransfer.2018.01.088

Suresh S (2019) An experimental investigation on the effect of gravitational orientation on flow boiling performance in different channel sizes ranges from minichannels to microchannels. Heat Mass Transf 56:1–30

Tibirica CB, Ribatski G (2013) Flow boiling in micro-scale channels—synthesized literature review. Int J Refrig 36(2):301–324

Utaka Y, Hu K, Chen Z, Morokuma T (2018) Measurement of contribution of microlayer evaporation applying the microlayer volume change during nucleate pool boiling for water and ethanol. Int J Heat Mass Transf 125:243–247

Van Dyke AS, Collard D, Derby MM, Betz AR (2015) Droplet coalescence and freezing on hydrophilic, hydrophobic, and biphilic surfaces. Appl Phys Lett 107(14):141602

Vermaak M et al (2020) Experimental and numerical investigation of micro/mini channel flow-boiling heat transfer with non-uniform circumferential heat fluxes at different rotational orientations. Int J Heat Mass Transf 158:119948

Vlachou MC, Karapantsios TD (2018) Effect of channel inclination on heat transfer and bubble dynamics during subcooled flow boiling. Int J Therm Sci 124:484–495

Vontas K, Andredaki M, Georgoulas A, Miché N, Marengo M (2021) The effect of surface wettability on flow boiling characteristics within microchannels. Int J Heat Mass Transf 172:121133. https://doi.org/10.1016/j.ijheatmasstransfer.2021.121133

Wang G, Cheng P (2008) An experimental study of flow boiling instability in a single microchannel. Int Commun Heat Mass Transf 35(10):1229–1234

Wang J, Li F-C (2017) Experimental study on the characteristics of CHF and pressure fluctuations of surfactant solution flow boiling. Int J Heat Mass Transf 115:1004–1010
Wang G, Cheng P, Bergles AE (2008) Effects of inlet/outlet configurations on flow boiling instability in parallel microchannels. Int J Heat Mass Transf 51(9–10):2267–2281
Wang Y, Sefiane K, Bennacer R (2011) Investigation of boiling and bubble confinement in a high aspect ratio micro-channel. Appl Therm Eng 31(5):610–618
Wang J, Cheng Y, Li X-B, Li F-C (2019) Experimental and LBM simulation study on the effect of bubbles merging on flow boiling. Int J Heat Mass Transf 132:1053–1061
Wang B, He M, Wang H, Qiu H (2017) Flow boiling heat transfer in wettability patterned microchannels. In: 2017 16th IEEE intersociety conference on thermal and thermomechanical phenomena in electronic systems (ITherm), pp 759–766
Wei J, Pan L, Chen D, Zhang H, Xu J, Huang Y (2011) Numerical simulation of bubble behaviors in subcooled flow boiling under swing motion. Nucl Eng Des 241(8):2898–2908
Wojtan L, Revellin R, Thome JR (2006) Investigation of saturated critical heat flux in a single, uniformly heated microchannel. Exp Therm Fluid Sci 30(8):765–774
Wong K-C, Chong J-H (2015) Hydrodynamics and heat transfer prior to onset of nucleate boiling in a rectangular microchannel heat sink. Int Commun Heat Mass Transf 64:34–41
Wu HY, Cheng P (2004) Boiling instability in parallel silicon microchannels at different heat flux. Int J Heat Mass Transf 47(17–18):3631–3641
Wu J, Wang Y (2021) Liquid blockage and flow maldistribution of two-phase flow in two parallel thin micro-channels. Appl Therm Eng 182:116127
www.ieee.org and https://irds.ieee.org7
Yan Q, Jia L, An Z, Peng Q (2019) A comprehensive criterion for slug-annular flow transition based on flow boiling of R134a in microchannels. Int Commun Heat Mass Transf 105:1–9
Yang B, Sarafraz MM, Arjomandi M (2019) Marangoni effect on the thermal performance of glycerol/water mixture in microchannel. Appl Therm Eng 161:114142
Yin L, Jia L, Guan P, Liu D (2014) Experimental investigation on bubble confinement and elongation in microchannel flow boiling. Exp Therm Fluid Sci 54:290–296
Yin X, Tian Y, Zhou D, Wang N (2019) Numerical study of flow boiling in an intermediate-scale vertical tube under low heat flux. Appl Therm Eng 153:739–747
Youn YJ, Muramatsu K, Han Y, Shikazono N (2015) The effect of initial flow velocity on the liquid film thickness in micro tube accelerated slug flow. Int J Multiph Flow 73:108–117
Yu DI et al (2015) Wetting state on hydrophilic and hydrophobic microtextured surfaces: thermodynamic analysis and X-ray visualization. Appl Phys Lett 106(17):171602
Yuan B, Zhang Y, Liu L, Wei J (2019) Experimental research on subcooled flow boiling heat transfer performance and associated bubble characteristics under pulsating flow. Appl Therm Eng 157:113721
Yuan B, Zhang Y, Liu L, Wei J (2020) Flow boiling heat transfer and associated bubble behaviors over backward-and forward-facing steps. Exp Therm Fluid Sci 122:110300
Zhang H, Mudawar I, Hasan MM (2002) Experimental and theoretical study of orientation effects on flow boiling CHF. Int J Heat Mass Transf 45(22):4463–4477
Zhang T, Cao B, Fan Y, Gonthier Y, Luo L, Wang S (2011) Gas–liquid flow in circular microchannel. Part I: influence of liquid physical properties and channel diameter on flow patterns. Chem Eng Sci 66(23):5791–5803
Zhang S, Yuan W, Tang Y, Chen J, Li Z (2016) Enhanced flow boiling in an interconnected microchannel net at different inlet subcooling. Appl Therm Eng 104:659–667
Zhang Z, Li L, Xie W, Wang H (2020) Experimental study of bubble formation process on the micro-orifice in mini channels. Exp Therm Fluid Sci 117:110144
Zhang L, Liu L, Liu H, Zhou X, Chen D (2021) Experimental investigation on sliding bubble coalescence of subcooled flow boiling in rectangular narrow channel. Int J Heat Mass Transf 165:120681
Zhou K, Coyle C, Li J, Buongiorno J, Li W (2017) Flow boiling in vertical narrow microchannels of different surface wettability characteristics. Int J Heat Mass Transf 109:103–114
Zhuan R, Wang W (2012) Flow pattern of boiling in micro-channel by numerical simulation. Int J Heat Mass Transf 55(5–6):1741–1753